Experimental Measurement of Stiffness with Magnetic Resonance Elastography for in vivo Healthy Human Brains

Honors Research Thesis

Presented in partial fulfillment of the requirements for graduation
with honors research distinction in Electrical and Computer Engineering
in the undergraduate colleges of The Ohio State University

By

Sangmin Cha

The Ohio State University

2014

Research Co-Advisors :

Dr. Bradley D. Clymer, Electrical and Computer Engineering

Dr. Arunark Kolipaka, Department of Radiology

DEDICATION

To the people who have supported me throughout my life

ACKNOWLEDGEMENTS

First and foremost, I would like to express my deepest appreciation to my advisors, Dr. Bradley Clymer and Dr. Arunark Kolipaka. Your support has led to the achievement of my first research thesis; without your encouragement, I could not have finished this thesis. Thank you once again for your patience and wisdom.

I would also like to pay respect and many thanks to my parents for giving me the opportunity to come study in America. By having your full support and sacrifice, I have always learned how to cultivate myself for the better.

I want to thank my brother and sister, respectively, Joohwan Cha and Soonyoung Cha. Since I was little, you always have had my back and helped raise me for who I am now. I am incredibly thankful for your support no matter what circumstances. Both of you were the reason why I was able to continue school and finally graduate. I cannot express enough gratitude for the financial sacrifices you both have made as well as giving me the mental support. I will most definitely make it up to you my entire life.

Then my special gratitude goes towards my sister, Iris Cha. Sis, thank you for ongoing support and love. You have always been there for me whenever I had needed your help. I promise you I will one day return the support that you gave to me and I will never forget what you have done for me.

Finally, I would like to express my thanks to my fiancé, Semi Jang. Since the first time we met, you have been always there for me and supported me. You have always loved me for who I am. For every slump and struggle that I had, you gave me the hope and courage to move on. Importantly, you always helped me up when I fell. I am grateful that I am given this opportunity with my first thesis to show my gratitude towards you. I was extremely lucky to have met you and from now on forward, I wish that you will spend your life in happiness with me.

LIST OF TABLES

LIST OF FIGURES

TABLE OF CONTENTS

CHAPTER 1

Introduction

There are multiple studies indicating that progression in age leads to the reduction of stiffness in the brain. This reduction of elasticity involves the loss of neurons and oligodendrocytes which can also lead to various brain diseases. For instance, it is known that the degeneration of white matter including demyelination, destruction of axons, as well as disruption of the glial matrix has been strongly correlated to the development of neurological disorders not to mention brain diseases.

Now, brain diseases are among the leading causes of death or disability and it is known to be a daunting task to diagnose this neurological disorder due to the dangers and complexity of brain surgery. One of the common methods employed for diagnosis of brain diseases, is the use of magnetic resonance imaging (MRI) because it is noninvasive. Although many diagnostic imaging techniques such as computed tomography (CT), ultrasound (US), and MRI have emerged, these radiographies cannot easily assess the brain's mechanical property like magnetic resonance elastography (MRE).

MRE is an MRI based technique that is capable of estimating the stiffness of soft tissues. Currently, MRE is used as a clinical diagnostic tool for staging liver fibrosis ruling out the need for liver biopsies. This technique is known to be safe and reliable while also carrying an enormous potential for the diagnosis of diseases in all parts of the human body including the brain.

For our research, we chose the brain specifically with use of the MRE to estimate the average of stiffness in healthy human brains with progression of age. Our first goal for this study was to measure the mean isotropic stiffness of the whole brain as well as the specific regions of the corpus callosum and the centrum semiovale. We chose only healthy participants of different age groups to find a strong correlation between the brain stiffness with regard to age since it is ideal to understand the change in stiffness of healthy individuals first. Finally, our next goal was to estimate the anisotropic stiffness in the same regions of interest like the isotropic stiffness and find the difference between the two results.

Regarding the ROIs (regions of interest) of this study, we have chosen the whole brain as one of the regions of interest to find a general link between the brain stiffness and age progression. Corpus callosum was chosen as one of our regions of interest since it plays an important role in the communication of the two hemispheres of the brain and the damage to this area is known to be a leading cause of traumatic brain injury. Furthermore, the centrum semiovale was important in our study since it consists of neural fibers such as cortical projection fibers, cortical fibers, and association fibers. It is known that increase in age is strongly associated with the atrophy of neuronal fibers which is why it was critical that we focus on the centrum semiovale and the corpus callosum to find a connection with age and damage to neural fibers.

1.1. Statement of the Problem

Most biological tissues are anisotropic in nature because they have structured fibers and exhibit different structural integrity in the direction of the fibers compared to transverse to them.

Therefore, identifying the fiber tracks and determining the anisotropic stiffness is very important in understanding the remodeling that occurs in these soft tissues during different pathological conditions. Since the brain is anisotropic in nature, the information of its fiber tracks is needed in order to measure the stiffness of the desired areas in the brain. This information can be acquired by the clinical standard diffusion tensor imaging (DTI) technique that measures the diffusion of water molecules in the tissues [4][5]. Recently, Romano et al has demonstrated the use of DTI to track the fibers in the brain and applying MRE to estimate anisotropic stiffness, and this is known as waveguide elastography [10].

1.2. Organization

In the following Chapter, the fundamental concepts of MRI, DTI and MRE are explained.

Chapter 3 describes the theories that are used to estimate the isotropic and anisotropic stiffness of the soft tissue.

In Chapter 4, the materials and methods such as subjects, diffusion tensor imaging, MRE acquisition, image analysis and region of interests for this brain MRE research are presented.

In Chapter 5, the results for the isotropic and anisotropic stiffness of the whole brain, corpus callosum, and centrum semiovale in different ages are stated.

Chapter 6 discusses the observed results along with suggestions to possible solutions of problems that were encountered during the study.

Finally, Chapter 7 concludes this study with the observed results and discussion.

CHAPTER 2

BACKGROUND

In this chapter, we give an overview of magnetic resonance imaging (MRI) and diffusion tensor imaging (DTI) and how magnetic resonance elastography (MRE) is performed in using these techniques.

2.1. Magnetic Resonance Imaging

Magnetic Resonance Imaging (MRI) is a non-invasive method of investigating the internal structure and function of the body. Nonionizing electromagnetic radiation is used in MRI, and it is known to be nonhazardous. MRI applies radio frequency (RF) radiation with controlled magnetic fields in order to obtain anatomic cross-sectional images of the body in any direction. By placing the patient into the strong magnetic field, the nuclei of atoms such as hydrogen in the body are aligned with the magnetic field, and later a RF signal is applied. Then, a radio wave receiver detects the energy released from the body and uses it to construct the MR images [1].

2.1.1. Physical bases of MRI

Nuclei of all atoms consist of two particles, protons and neutrons. All protons and neutrons are in motion and spin about their axis. Although there are some atoms composed mostly of nuclei that contain an even number of protons and neutrons without a spin or a magnetic moment, some nuclei possess an odd number of protons and neutrons, especially

hydrogen. Nuclei with an odd number of these particles have a nuclear spin and a magnetic moment [2]. The nuclei with an unpaired proton or neutron that have net spinning charge are suitable for MRI because the electrical charge of the spin creates a magnetic field in these nuclei; this allows the nuclei to act as magnetic dipoles [1].

Hydrogen is the most abundant atom in the human body, usually in the form of water. This atom is also MR sensitive because hydrogen nucleus contains an unpaired proton and acts as a magnetic dipole. In the absence of an external magnetic field, the magnetic dipoles of a group of hydrogen atoms are randomly oriented and generate a zero net magnetization. In a case where a static magnetic field, H_o, is introduced to the sample, the hydrogen nuclear spin axes line up relative to the direction toward the magnetic field, resulting in a net magnetization. The magnetization can go either of two ways: one can be in the direction of the magnetic field (parallel to the magnetic field H_o with spin up), or it can be anti-parallel to the magnetic field (spin down). The orientations represent a lower energy state and a higher energy state of the dipole, respectively. In absorbing or releasing a particular amount of energy a nucleus can transition from one energy state to another (resonance). The energy can be regained or supplied in an electromagnetic form in the RF portion of the electromagnetic spectrum [1].

When H_o is applied, the individual dipoles' North and South poles do not align with the direction of the magnetic field. Rather, the axes of spinning dipoles have a slight tilt with a precession (oscillation or wobble) toward a position, parallel to the flux of the external magnet (**Figure 2.1**). The rate/frequency of the precession is called the resonant or Larmor frequency and it is proportional to the strength of the magnetic field that is applied,

$$\omega_o=\gamma H_o \qquad (2\text{-}1)$$

where ω_o is known as resonant frequency, γ is the gyro magnetic ratio, and H_o is the applied field. One Tesla is 10,000 times a Gauss and the earth's magnetic field is 0.25G. In one tesla, the Larmor frequency of hydrogen is about 42.58 MHz. MR imaging of humans uses magnetic field strengths that range from 0.1 to 7.0T [1].

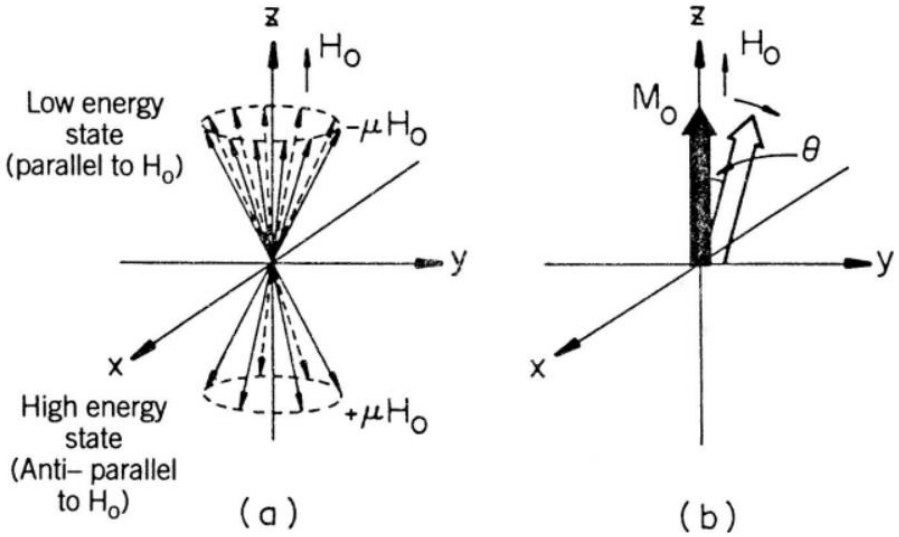

Figure 2.1. Spins in a magnetic field H_o. (a) The spins precess about H_o in two energy states. More spins are usually aligned in the direction of H_o at room temperature. (b) The net spin magnetization vector M_o is given by $M_o = \sum \mu$. Note that at thermal equilibrium M_o is along H_o. This spin magnetization can be rotated or flipped at angle θ by addition of an external magnetic field such as short duration rf pulse. Adapted from "Foundations of Medical Imaging," by Z.-H. Cho, J. P. Jones, M. Singh, 1993, p. 246. Copyright 1993 by John Wiley & Sons, Inc.

The combined effect of the two energy states results in a weak net magnetization vector (M) (a net magnetic moment), parallel to the applied magnetic field. When energy from a RF antenna coil, in the form of an electromagnetic wave is directed toward tissue with hydrogen nuclei (protons) aligned in the z-axis from H_o, the protons in the tissue with a Larmor frequency matching the electromagnetic wave can absorb energy. The magnetic dipoles then rotate away from the H_o direction due to torque between H_o and individual dipole moments [1].

When the RF field H_1 is applied longer, the angle of the tip of the magnetization becomes greater. If a pulse has enough duration, it will flip the net tissue magnetization vector into a x-y plane (transverse plane), which is perpendicular to the z-axis (longitudinal alignment). This

causes the precession of protons in phase, and the maximum RF signal is induced in a receiver coil (**Figure 2.2**) [1].

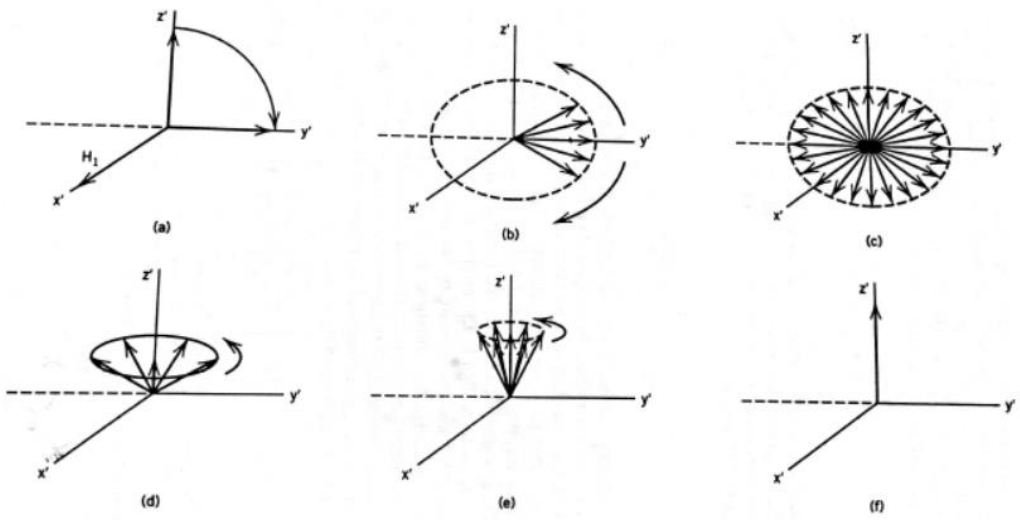

Figure 2.2. Sequential behavior of the spin relaxation processes. (a) The spin magnetization is flipped by an RF pulse H1. (b) The spins undergo dephasing due to the spin-spin relaxation and field inhomogeneity. (c) When fully dephased the FID signal decays to zero as the spins lose phase coherency. (d), (e), and (f) represent T_1 spin relaxation processes which lead to the recovery of the spins to the original equilibrium state via the spin-lattice relaxation process. Adapted from "Foundations of Medical Imaging," by Z.-H. Cho, J. P. Jones, M. Singh, 1993, p. 248. Copyright 1993 by John Wiley & Sons, Inc.

2.1.2. Signal losses over time

After the RF pulse is turned off, two relaxation processes occur by dispersing nuclear spin energy through neighboring lattices and spins and the energy is detected as a signal by a RF receiver coil [1]. One of the relaxation processes, known as longitudinal relaxation or T_1, is caused by the return to thermal equilibrium. This aligns the rotating spin magnetization back to the z-axis (longitudinal alignment) from the x-y plane (transverse plane) with the time for this process known as the spin-lattice relaxation time or T_1; that is, the spins return to the low-energy state (**Figure 2.2**). At the same time, the transverse components of the magnetization decrease to a value of zero with the decay time known as spin-spin relaxation time or T_2 by dephasing the

spins. T_2 is primarily due to dephasing interference between dipoles [2]. Fundamentally, in order to separate the several tissues by contrast resolution, both T_1 and T_2 can be exploited to produce images. Since the strength of the external magnetic field controls the Lamor frequency, MRI can localize specific parts of the body and create a 3-D image, by locally controlling the strength of the magnetic field [1].

Three gradient coils generate the gradient magnetic fields in the bore of an MRI scanner where the subject is placed. A linear gradient field produced by each coil deflects and opposes the magnetic flux in 3 orthogonal directions to define individual volumes of tissues that are affected by magnetic fields of particular strength. Subdividing the local magnetic fields causes the hydrogen protons to align within a certain voxel to the same resonant frequency. When a RF field with a range of frequencies is applied, a voxel of tissue that is tuned to a particular frequency is excited. This is known as selective excitation. When the RF pulse is turned off, the particular frequency is emitted by the excited voxel, and so it can be identified and localized. The slice thickness is determined by the bandwidth of the RF field and the magnitude of slice-selection gradient. In decreasing the bandwidth of the RF pulse or increasing the strength of the gradient, slice thickness can be reduced [1].

The spins in the selective slice are dephased by relaxation processes after the RF pulse is turned off. This dephasing causes signal loss by interference, and therefore the spins need to be rephased for the signal detection [2].

The magnetic field B_o has been assumed to be uniform in the previous analysis of MR imaging. However, the resonant frequency across a sample is not uniform in practice due to main field inhomogeneities, susceptibility-induced field variations, and chemical shift. These

deviations are often known as off-resonance conditions since the frequency is usually referred with respect to the resonant frequency ω_o [3].

The magnet technology has been advanced to generate high-field magnets with enough field uniformity over a large volume. The overall uniformity can be improved by the fields generated by auxiliary shim coils. The main field inhomogeneity is expressed in terms of parts per million (ppm) of the main magnetic field B_o [3].

The differences of the resonant frequency can still exist even with a perfect magnet due to sample-induced B_o variation. Differences in bulk magnetic susceptibility χ in the sample cause the variations. This susceptibility difference and geometry determine the amount of field inhomogeneity typically on the order of a few ppm. Around the boundaries between two materials that have different susceptibilities, for example air ($\chi > 0$) and tissue ($\chi < 0$), the inhomogeneity is the highest. This effect is observed in body parts such as lungs, abdomen (intestinal gases), and head (sinuses) [3].

Chemical shift is another source that causes the frequency offset. The electronic shielding reduces the magnetic field which is experienced by the nucleus. The effective shielded field B_{sh} at the nucleus is

$$B_{sh} = B_0(1 - \sigma) \tag{2-2}$$

where σ is a shielding constant that represents the small field contributed by the electrons. Thus, a small shift in the resonant frequency results and the resonant frequency is

$$\omega = \gamma B_{sh} = \gamma B_0(1 - \sigma) \tag{2-3}$$

$$f = \frac{\gamma}{2\pi} B_{sh} = \frac{\gamma}{2\pi} B_0(1 - \sigma) \tag{2-4}$$

This displacement in the resonant frequency depends on the chemical environment of the nuclei and is expressed in terms of ppm. For instance, a chemical shift of the hydrogen in fat is

approximately 3.5 ppm relative to the hydrogen in water. This means that the frequency shift is about 150 Hz at 1 T. Therefore, even though multiple species of chemical shift may generally exist together, the chemical shift can be viewed as "discrete" inhomogeneity [3].

The space-dependent resonance offset introduced by field inhomogeneities can cause distortions and artifacts in images since the resonant frequency is proportional to the applied field. The effects of inhomogeneities on the signal without gradient fields are analyzed here first. If $B_0 + E(r)$ is the z-component of the magnetic field where $E(r)$ is the nonuniformity of the field, $\omega_E(r) = \gamma E(r)$ is then the nonuniformity in frequency. Now, the received baseband signal can be written as

$$s(t) = \int_{vol} m(r) e^{-i\omega_E(r)t} e^{-t/T_2(r)}\, dV \tag{2-5}$$

where $e^{-i\omega_E(r)t}$ is the phase factor that indicates a frequency distribution over the object causing loss of phase coherence of the spins. The destructive phase dispersion is caused by this frequency distribution and exhibits more distinct amplitude decay when compared to the intrinsic T_2 processes as well as the signal's phase errors (**Figure 2.3**). The phenomenon of this destructive phasing is typically called T_2* decay with T_2* as the effective reduced time constant. Individual spin experiences a decay that depends on its T2 value. However, the collective signal over all spins in the volume or over the resonant frequency distribution is the one that decays with T2* time constant. The signal decay is not exponential, but is dependent on the distribution of $E(r)$. For instance, if there is a linear field inhomogeneity across a rectangular object, the decay envelope is a sinc function. A gradient field is generally a much stronger form of a field inhomogeneity and therefore the decay of the signal envelop is faster in its presence (**Figure 2.3**) [3].

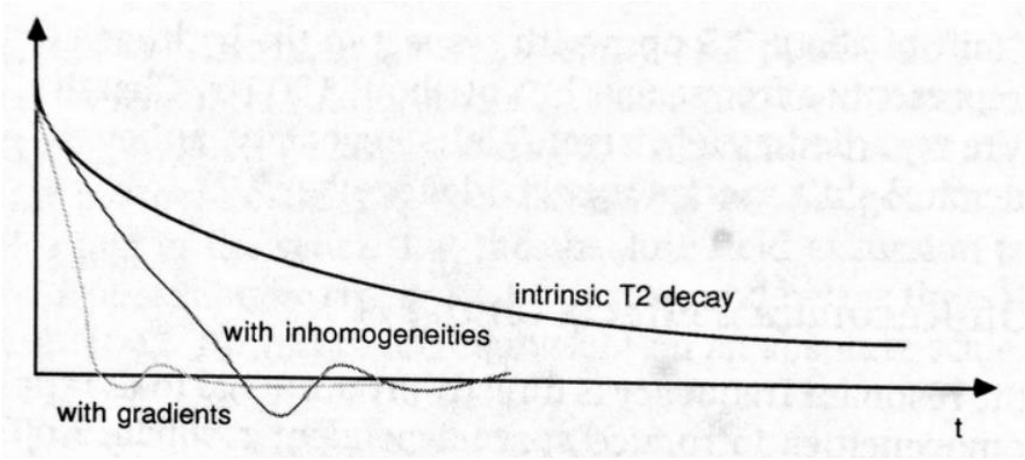

Figure 2.3. Three Types of Signal Decay Envelopes: 1) intrinsic T2, 2)with inhomogeneities, and 3) with gradient fields. Adapted from "Principles of Magnetic Resonance Imaging," by D. G. Nishimura, 2010, p. 135. Copyright 2010 by Dwight G.

2.1.3. Signal phase recovery

There are several types of echo sequence techniques that can rephase the spins, thereby improving the strength and coherence of the signal for the data acquisition. Gradient echo recall is the simplest type of MRI sequence. This echo sequence is produced by using a pair of bipolar gradient pulses. Phase can also accumulate from applied gradient fields as well as off-resonance sources when the reference frame rotates at the center of frequency ω_o.

The source's signal phase offset is described here:

$$\phi(x,y,z,t) = \int_0^t \omega(x,t,x,\tau)d\tau \qquad (2\text{-}6)$$

$$= \omega_E(x,y,z)t + \omega_{cs}t + \gamma \int_0^t G(\tau)\cdot r\, d\tau$$

where $\omega_E(x,y,z)t$ and $\omega_{cs}t$ are related to the constant phase accrual with the time from inhomogeneity and chemical shift correspondingly, and $\gamma \int_0^t G(\tau)\cdot r\, d\tau$ is the term of the

controllable phase accrual from the gradient fields. In the case of a perfect main field with no chemical shift: $\omega_E(x,y,z) = 0 \; and \; \omega_{cs} = 0$ [3],

$$\phi(x,y,z,t) = \gamma \int_0^t G(\tau) \cdot r \, d\tau \tag{2-7}$$

A gradient echo is said to occur when $\phi(x,y,z,t) = 0$ and is achieved by dephasing the spins with a negatively pulsed gradient causing the spin phases to warp over space. The received signal decays quickly compared to the intrinsic T_2 of the object. The gradient field begins to reverse at time τ and the phase warping (time t = 0 to τ) starts to unwind due to precession of the spins that are going from a slower frequency to a higher frequency. When the spin starts to attain its coherence again, the echo is formed (**Figures 2.4 & 2.5**) [3].

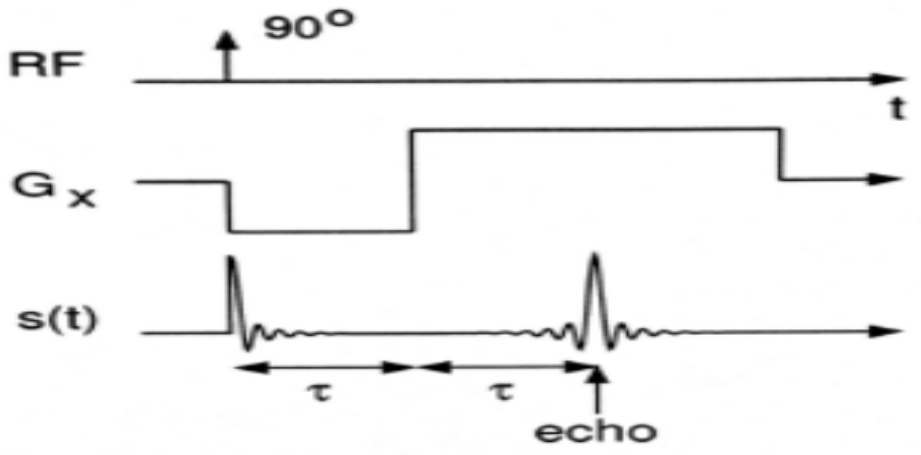

Figure 2.4. Gradient Echo Sequence: The echo peaks at 2τ. Adapted from "Principles of Magnetic Resonance Imaging," by D. G. Nishimura, 2010, p. 135. Copyright 2010 by Dwight G.

The spin vector becomes rephased maximally and the gradient echo peaks at t = 2τ, which is the point in which the cumulative area of the gradient wave form equals 0. In the case where t > 2τ, the phases disperses again (**Figure 2.4**). Another viewpoint of the phase progression is given by a plot of the phase as a function of time for three different x positions

(**Figure 2.5**). The gradient echo also has multiple names, being: gradient-reversed echo, gradient-refocused echo, gradient-recalled echo or field echo [3].

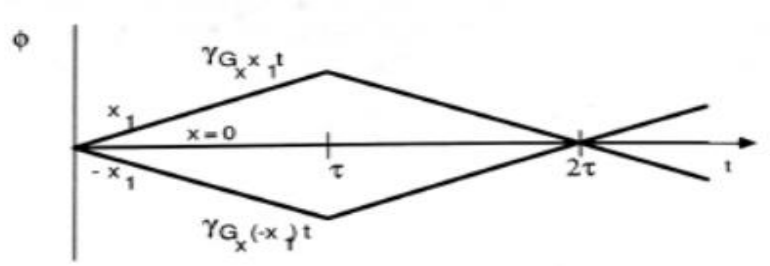

Figure 2.5. Phase Plot: Gradient Echo-Phase progression of spins at x_1, 0, and $-x_1$. Spin at x_1 is at higher frequency from time 0 to τ (gains phase), lower frequency from τ (loses phase). At time 2τ, spins have rephased. Adapted from "Principles of Magnetic Resonance Imaging," by D. G. Nishimura, 2010, p. 135. Copyright 2010 by Dwight G.

An alternative rephasing method is called the spin echo sequence (**Figure 2.6**) [3]. According to the figure 5, a 90˚ RF pulse is applied along the x direction, and the magnetization vector (M) of the spins flips to the x-y (transverse) plane. The added gradient fields or the field inhomogeneity make the spins start dephasing over the time (some spins become slower and others speed up). A following 180˚ RF pulse is applied along the x´-axis or y´-axis to flip the dephased spin vectors 180˚ around the x´-axis or y´-axis, respectively (faster spins are behind in phase, slower spins are ahead in phase). Now, the rephasing of the spins starts occurring by continuing the precessions with the same direction (the previously slower spin vectors become ahead of the previously faster ones). A spin echo is completed at t = 2τ when the spins are finally rephased [2].

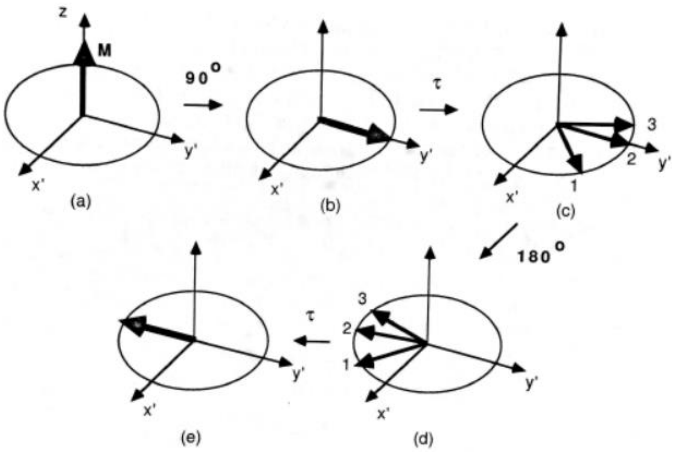

Figure 2.6. Spin Echo Generation: Following a 90˚ excitation pulse (a-b), the spin vectors begin to fan out and dephase because of precessional frequency differences (c), at time τ, a 180˚ excitation rotates all the spins about the x-axis (d). The spin vectors continue to precess at their slightly different frequencies, rephasing at time 2τ (e). Adapted from "Principles of Magnetic Resonance Imaging," by D. G. Nishimura, 2010, p. 138. Copyright 2010 by Dwight G. Nishimura.

The following analogy of a spin echo can help with understanding: In this case, the spin echo phase is similar to a track race and the runners (spins) with different constant foot speeds (resonant frequencies) start at t = 0 (in phase) which is the starting line of a circular track (transverse plane). When the race begins, the faster runners outrun the slower runners and "dephase." Then at some point of the race, the runners are distributed around the track in various positions due to their individual speeds. At time τ-, with 180 degrees excitation, the position of the runners is reversed with faster runners most behind and slower runners most ahead. However, since the runners continue to run at their own constant speeds, the faster runners will eventually outrun the slow runners again after another time τ. Therefore at time 2τ, all runners come to the same point of the starting line, in phase [3].

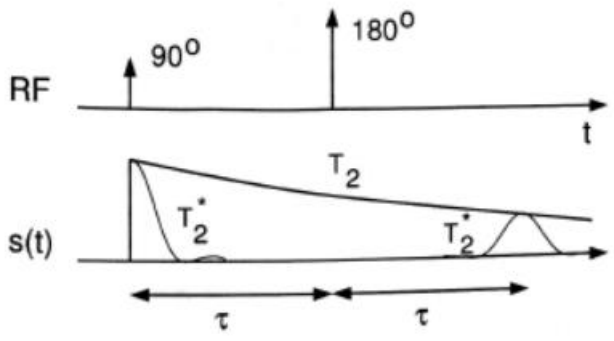

Figure 2.7. Signal envelope after the 90˚ pulse shows T_2* decay. At time 2τ, a spin echo forms, attaining an amplitude determined by the intrinsic T_2 of the sample. The decay after 2τ also shows the T_2* behavior. Adapted from "Principles of Magnetic Resonance Imaging," by D. G. Nishimura, 2010, p. 139. Copyright 2010 by Dwight G.

In looking at the 90-180 degree sequence, the time signal displays an initial T_2* decay after the 90 degree pulse (**Figure 2.7**). The T_2* decay (dephasing phase) is caused by the inhomogeneity of the field, and when considering a uniform T_2, it conceals the intrinsic T_2 decay of the object. After the initial T_2* characteristic, a spin echo follows the 180 degrees pulse, and hereon after another T_2* reforming waveform is displayed. Here, the T_2 decay is non-reversible although the 180 degree RF pulse reverses the dephasing effects because of the inhomogeneity. Consequently, at time 2τ, the spin echo amplitude is dependent upon the intrinsic T_2 [3].

In another analogy, before the 180 degree pulse, the dephased spin vectors form a "pancake" of magnetization vectors, spreading out over the entire transverse plane. 180 degree pulse then flips the pancake over at a particular axis. After the flip, due to spin refocusing, the echoing of the signal displays a time-reversed version of the signal that followed the 90 degree pulse. The 180 degree RF pulse (pancake flipper) clearly plays a central role in spin-echo formation and is commonly called the time-reversal pulse, phase reversal pulse, or refocusing pulse [3].

2.1.4. Motion sensitive MRI

As we discussed previously, magnetic field gradients are mainly used for spatial encoding. However, the gradients are also used for other purposes. They are included into a pulse sequence to make MRI signals sensitive to motion. The sensitivity of magnetic resonance imaging (MRI) to motion makes it possible to be used for noninvasive image of physiological motion. There is a wide range of applications of MRI in medical diagnosis. There are two significant MRI applications using the motion sensitivity: (1) Diffusion tensor imaging (DTI)

and (2) Magnetic resonance elastography (MRE). Here we discuss gradients used to sensitize the MR image to motion is a diffusion-weighting gradient [8].

A diffusion-weighting gradient is composed of two lobes with the same area. The polarity of these two lobes depends on the type of a pulse sequence that the gradient is incorporated into. In case of spin-echo-based sequences, the two lobes of the gradient have the same polarity with the equal area, and each lobe is placed at either side of an 180˚ refocusing RF pulse (**Figure** 2.**8**). However, in pulse sequences based on gradient echoes, the polarities of the two lobes are opposite, and the lobes are usually linked together with the zero net area (**Figure** 2.**8**). The diffusion-weighting gradient is typically known as a bipolar gradient although it is a unipolar in the case of spin-echo-based sequences [8].

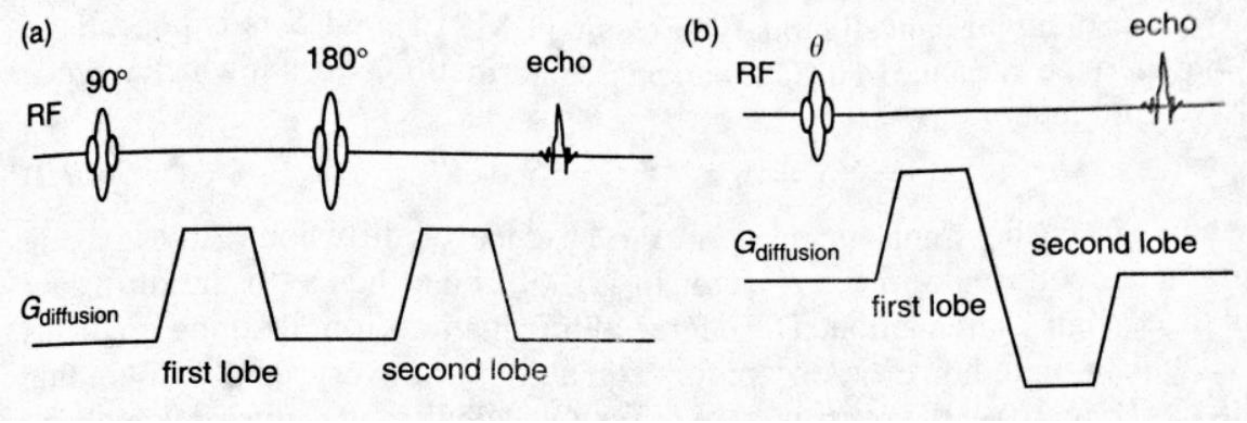

Figure 2.8. Examples of diffusion-weighting gradient waveforms used in a (a) spin-echo pulse sequence and (b) gradient-echo pulse sequence. Adapted from "Handbook of MRI Pulse sequences," by M. A. Bernstein, K. F. King, and X. J. Zhou, 2004, p. 275. Copyright 2004 by Elsevier Inc.

Brownian motion during the data acquisition can result in loss of proton MRI signals when the diffusion-weighting gradient is used in a pulse sequence. If the spins within a voxel are in the same location during the two lobes of the diffusion-weighting gradient, the dephasing caused by the first lobe will be canceled by its second lobe, and therefore there is no signal attenuation. On the other hand, if the spins within a voxel are moved to the different location due

to random or Brownian motion during the two lobes, the dephased spins by the first lobe will not be rephased by the second lobe, and thus it will cause MRI signal loss. As a result of this signal loss, the objects that have motion will be darker compared to ones without motion in the MRI image [8].

2.2. Diffusion Tensor Imaging

The diffusion MRI or DTI is a method that allows measuring of the Brownian motion of water molecules in biological tissues. The DTI method is used mostly to visualize the white matter of the brain and has been tremendously popular in neuroscientific studies including traumatic brain injury, multiple sclerosis, schizophrenia etc. because of its ability to image the complicated anatomy of the neural fiber tracks in the brain [4].

For the diffusion of water molecules in a glass of pure water, the molecules diffuse equally in all directions (isotropic). On the other hand, the diffusion in biological tissues often varies with directions (anisotropic). In the white matter of the brain, the cellular membranes, packing of axons and myelination cause diffusion anisotropy by limiting mobility of water molecules in some directions. The underlying tissue orientation can be described by this diffusion anisotropy [4].

The basic principles of DTI combine the MRI principles with the anisotropic diffusion concepts to encode the effects of molecular diffusion in the MR signal by using bipolar magnetic field gradients. This molecular diffusion refers to Brownian motion that is the random motion of molecules caused by their thermal energy. The underlying foundation of MRI makes it a powerful tool due to its ability to help us examine tissues at a microscopic level despite the basic image resolution. Some of the examples are: 50 msec of diffusion times, water molecules are

able to travel on average of 10 micrometers, the three dimensional application allows the examination of numerous tissues such as macromolecules, cell membranes, or fibers (**Figure 2.9**) [5].

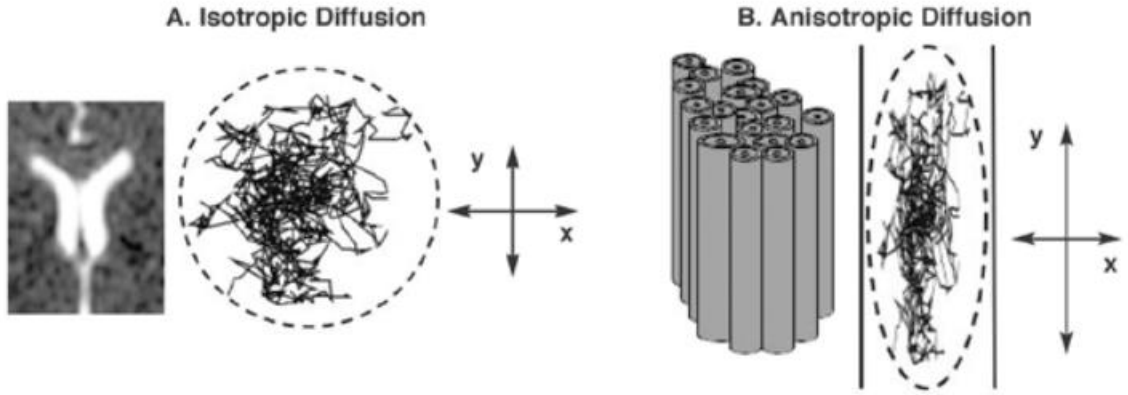

Figure 2.9. Isotropic and anisotropic diffusion. (A) Water molecules in the brain are constantly moving (i.e., in Brownian motion). When motion is unconstrained, as in the large fluid–filled spaces deep in the brain (i.e., the ventricles, as illustrated in the MR image on the left), diffusion is isotropic, which means that motion occurs equally and randomly in all directions. (B) When motion is constrained, as in white–matter tracts (illustrated on the right), diffusion is anisotropic, meaning that motion is oriented more in one direction than another (e.g., along the y axis rather than along the x axis). Adapted from " Using Magnetic Resonance Imaging and Diffusion Tensor Imaging to Assess Brain Damage in Alcoholics," by M. Rosenbloom, E. V. Sullivan, A. Pfefferbaum, 2004, National Institute on Alcohol Abuse and Alcoholism.

According to statistics, the image voxel of several mm in diffusion MRI follows the water molecule's displacement distribution in this voxel. Therefore, the study of the displacement distribution can lead to a better idea of the geometric organization as well as structure of tissues. Diffusion can be studied in vivo noninvasively in MRI. Moreover, with MRI's high resolution power, probing both superficial and deep organs is possible and MRI does not intervene or interfere with the process of diffusion [5].

In the anisotropic case, media may have a particular physical arrangement or obstacles may arise that limit the movement of molecules in certain directions. Since diffusion is a three-

dimensional process, if molecular mobility in tissues is variant by direction, range of motion during a time period is different for different directions. Repeating gradient motion procedure with different diffusion encoding directions allows fitting of surface of ellipsoid used to display the tensor data with images [5].

To fully describe isotropic diffusion with MRI, the diffusion coefficient (D) which is a scalar parameter is used. Diffusion causes the attenuation (A) of the MRI signal as explained before. This attenuation is dependent on D and "b factor" which is defined by the timing, amplitude, or shape of the gradient pulses used in the MRI sequence.

$$A = e^{-bD} \tag{2-8}$$

However, a single scalar coefficient cannot represent the diffusion with the involvement of anisotropy. In this case, a tensor (D) is required, and this characterizes the mobility of molecules along all different directions and correlation between them [5].

$$D = \begin{matrix} D_{xx} & D_{xy} & D_{xz} \\ D_{yx} & D_{yy} & D_{yz} \\ D_{zx} & D_{zy} & D_{zz} \end{matrix}, \qquad (D_{ij} = D_{ji}\ with\ i,j = x,y,z) \tag{2-9}$$

In a principal reference frame [x′, y′, z′] aligned with the diffusion properties, the off-diagonal terms of the tensor are zeroes and only its diagonal terms ($D_{x'x'}$, $D_{y'y'}$, $D_{z'z'}$) that characterize mobility of molecules along x′, y′, and z′, respectively exist. Now, the attenuation is:

$$A = e^{(-b_{x'x'}D_{x'x'} - b_{y'y'}D_{y'y'} - b_{z'z'}D_{z'z'})} \tag{2-10}$$

where $b_{x'x'}, b_{y'y'},\ and\ b_{z'z'}$ are from the b matrix related to the reference frame. However, since the measurements are generated in the reference frame of the gradients used in the MRI scanner and they usually do not match with the reference frame of the diffusion in a tissue, the coupling of the off-diagonal elements($D_{ij}, b_{ij}\ with\ i \neq j$) of the diffusion tensor and b matrix should also be considered in practice. The nondiagonal terms, D_{ij}, of the diffusion tensor are now expressed

in the frame of the MRI scanner and define the correlaxtion between molecular displacements in perpendicular directions. Now, the attenuation becomes:

$$A = e^{(-b_{xx}D_{xx}-b_{yy}D_{yy}-b_{zz}D_{zz}-2b_{xy}D_{xy}-2b_{xz}D_{xz}-2b_{yz}D_{yz})} \quad (2\text{-}11)$$

Therefore, when diffusion-encoding gradient pulses are used along only one direction (i.e. x-axis), the signal attenuation is affected by the diffusion along this direction as well as possible contribution from other directions (i.e. y-axis and z-axis) [5].

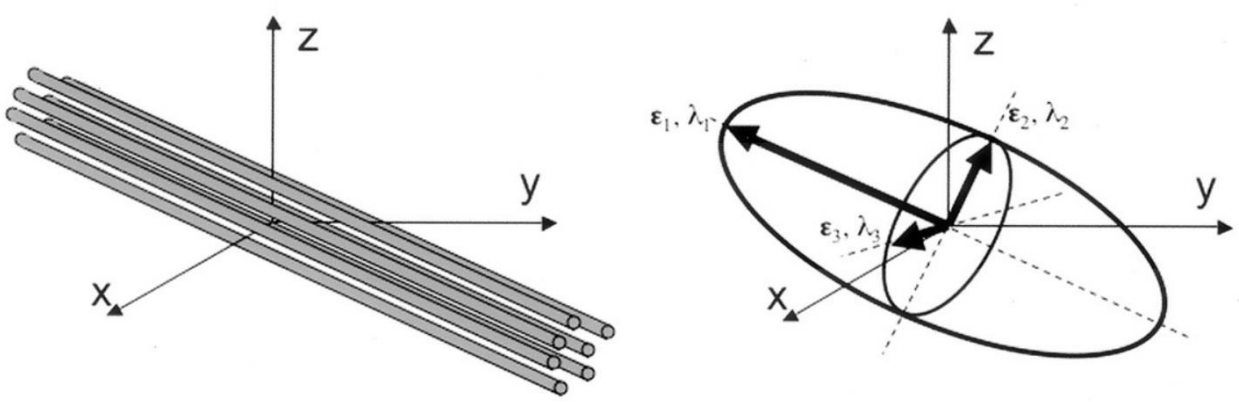

Figure 2.10. *Left,* Fiber tracts have an arbitrary orientation with respect to scanner geometry (x, y, z axes) and impose directional dependence (anisotropy) on diffusion measurements. *Right,* The three-dimensional diffusivity is modeled as an ellipsoid whose orientation is characterized by three eigenvectors ($\varepsilon_1, \varepsilon_2, \varepsilon_3$) and whose shape is characterized three eigenvalues ($\lambda_1, \lambda_2, \lambda_3$). The eigenvectors represent the major, medium, and minor principle axes of the ellipsoid, and the eigenvalues represent the diffusivities in these three directions, respectively. Adapted from "Diffusion Tensor Imaging of Cerebral White Matter: A Pictorial Review of Physics, Fiber Tract Anatomy, and Tumor Imaging Patterns," by B. J. Jellison, A. S. Field, J. Medow, M. Lazar, M. S. Salamat, and A. L. Alexander, 2004, 25:356-369, AJNR Am J Neuroradiol.

Since displaying tensor data with images is difficult, the theory of diffusion ellipsoids was introduced. The three-dimensional representation of the diffusion distance enclosed by molecules in space within a T_d (diffusion time) is called an ellipsoid (**Figure 2.10**). These ellipsoids can be measured from the eigen diffusivities, $\lambda_1, \lambda_2, and\ \lambda_3$.

$$\frac{x'^2}{2\lambda_1 T_d} + \frac{y'^2}{2\lambda_2 T_d} + \frac{z'^2}{2\lambda_3 T_d} = 1 \quad (2\text{-}12)$$

The eigen diffusivities are the unidimensional diffusion coefficients of the medium in the direction of the main diffusion, whereas, x′, y′, and z′ represent the frame of the tensor's main

diffusion direction. Thus, the direction of the main diffusion in the voxel is provided by the main axis of the ellipsoid, and information of the degree of anisotropy and its symmetry is given by the ellipsoid's eccentricity. The distance of diffusion covered in this direction provides the length of the ellipsoids in any direction in space, and this means that the ellipsoid can be viewed as 3-D surface of constant mean squared displacement of the diffusing molecules [5].

In order to determine the diffusion tensor completely, the diffusion-weighted images along several directions of the gradient should be collected at first. The pulsed-gradient spin echo (PGSE) pulse sequence with echo planar imaging (EPI) readout is the common diffusion-weighted imaging (DWI) approach (**Figure 2.11**). A pair of gradient pulses are used for this pulse sequence and placed on both sides of the 180˚ refocusing pulse. One of the gradient pulses dephases the magnetization across the sample, and the other one rephases the magnetization. For non-diffusing molecules, the phases caused by the gradient pulses totally cancel, and the magnetization becomes maximally coherent. As a result, there is no signal attenuation from diffusion. On the other hand, for the coherent flow in the applied gradient direction, the net phase difference is relative to the displacement when the bulk motion leads to a change in the signal phase of different amounts per pulse. The displacement of diffusing water can be described by a distribution. Therefore, the different phases are accumulated by water molecules with the presence of diffusion gradients. MRI signals corresponds to the water molecules within a voxel of all magnetization components added together. Thus, signal attenuation caused by the phase dispersion from diffusion occurs. The strength of signal attenuation is dependent on the magnitude of diffusion weighting and molecular translation. The strength of the diffusion gradients, the time between the gradient pulses, and the duration of the gradients determine the amount of diffusion weighting. The large diffusion-weighting gradients cause DW MRI to be

very sensitive to subject motion. The phase and amplitude in the collected data can be caused by very small amount of motion. The attenuated image of given position is proportional to localized diffusion. Although in cases where there is a change in the diffusion gradient or spatial direction, the image intensity can be variable. Therefore, the changes are responsible by diffusion tensor models [6].

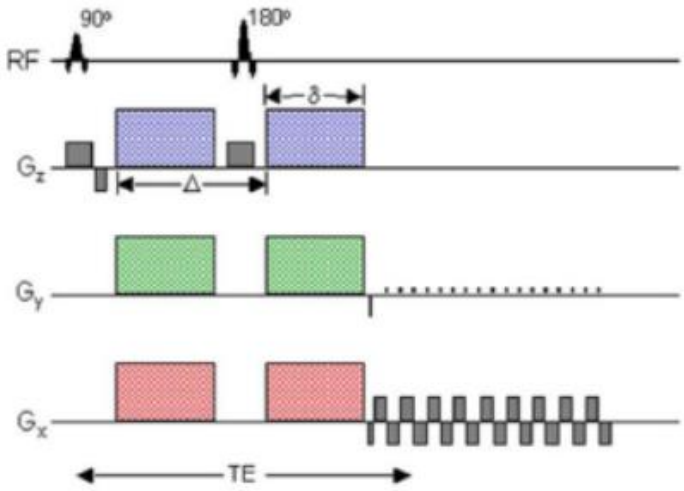

Figure 2.11. Schematic of a DW EPI pulse sequence. A spin echo is used to achieve diffusion-weighting from the gradient pulse pairs (colored). The imaging gradients are shown in grey. Diffusionweighting gradients can be applied in any arbitrary direction using combinations of Gx (red), Gy (green) and Gz (blue). Adapted from "Diffusion Tensor Imaging of the Brain," by A. L. Alexander, J. E. Lee, M. Lazar, and A. S. Field, 2007, 4(3): 316–329, Neurotherapeutics.

Second, by using the raw diffusion-weighted images, the diffusion tensor values can be estimated. The average diffusion and degree of anisotropy can be measured from the DT components. Now, the main direction of diffusivities in each voxel as well as the diffusion values related to these directions need to be determined. This is the same as finding the reference frame [x′, y′, z′] where only the diagonal terms of a tensor (D) which describes maneuverability of molecules along each direction and correlation between these directions are valid. Eigen-values and eigen-vectors related to associated diffusivities and directions of the main diffusion are given by these diagonal terms of the diffusion tensor [5].

There are three ways to analyze diffusion data and give information on microstructure and architecture of tissue for each voxel: (1) The mean diffusivity, (2) degree of anisotropy, and

(3) main direction of diffusivities. The overall presence of obstacles to diffusion and the overall mean-squared displacement of molecules can be described by the mean diffusivity. The degree of anisotropy is linked to the presence of oriented structures and shows how much displacements of molecules change in space. Finally, the orientation in the structures' space is related to the main direction of diffusivities (main ellipsoid axes). The DTI parameters, which are the mean diffusivity, degree of anisotropy, and main direction of diffusivities, can be obtained from the whole idea of the diffusion tensor [5].

2.3. Magnetic Resonance Elastography

Magnetic resonance elastography (MRE) is an MRI based technique and is a novel noninvasive technique to estimate the mechanical properties such as stiffness of soft tissues. Currently, MRE is a clinical diagnostic tool for staging liver fibrosis replacing the need for liver biopsies. MRE is safe, reliable, and it also has potential for diagnosis of diseases in all parts of the human body because disease processes such as cancer and inflammation seriously affect the mechanical properties of tissues. In utilization of the magnetic resonance imaging (MRI) technique, MRE is able to retrieve information regarding the stiffness of tissue by evaluating the propagation of mechanical (vibrational) waves that go through the tissues. There are generally three steps for this technique. The first step is to apply mechanical shear waves into the soft tissue, and then MR images that describe the propagation of the induced shear waves are collected by signal losses at vibrating locations. Post processing these images to estimate the wavelengths of the acoustic waves can be determined to assess tissue stiffness. Lastly, elastograms are generated, which are quantitative maps of tissue stiffness, from the processed shear wave images [7].

First of all, a source of motion is applied to tissues. External driver devices are usually used in MRE to generate the mechanical waves in tissues. The vibrations generated by the drivers typically have a single frequency within the audio range. For the driver devices, a signal generator triggered by and matched to the MR pulse sequence produces the electrical signal. An audio amplifier then amplifies the signal before it goes into the mechanical driver (**Figure 2.12a**). Several mechanisms of the drivers have been developed over the years. Three of the most common driver systems are electromechanical, piezoelectric-stack, and pressure-activated driver systems. The electromechanical driver system uses the magnetic field of the main MRI magnet and the Lorentz force to generate the vibrations (**Figure 2.12b**). For the piezoelectric-stack driver system, the piezoelectric property of certain materials determines the motion created by it (**Figure 2.12c**). Lastly, the pressure-activated driver system generates the vibrations required for MRE by using the motion of the voice coils in acoustic speaker systems (**Figure 2.12d**) [7].

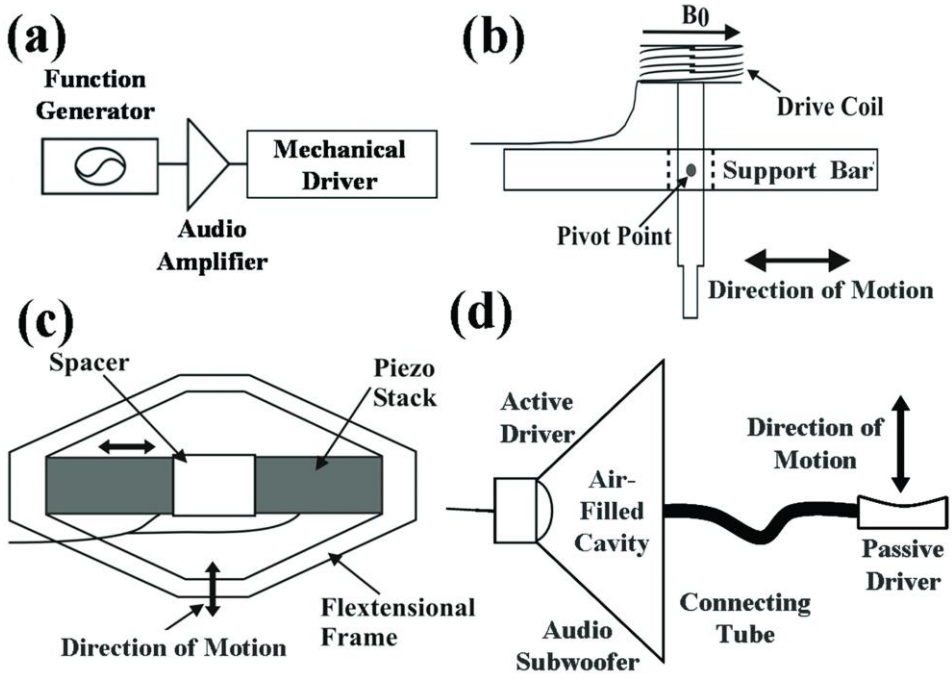

Figure 2.12. (a) Block diagram of the external driver setup. Examples of typical mechanical drivers include (b) electromechanical, (c) piezoelectric-stack, and (d) pressure-activated driver systems. Adapted from "Magnetic Resonance Elastography: A review," by Y. K. Mariappan, K. J. Glaser, and R. L. Ehman, 2010, 23(5): 497-511, Clin Anat.

The motion of tissue created by a driver with MRE can be measured by using the technique of phase-contrast MRI. The dynamic phase-contrast MRE technique was developed in which the phase of the MR images along with motion-encoding gradient pairs encodes the propagating shear waves in tissues. After harmonic motion is continuously induced in the soft tissue, an oscillating motion-encoding gradient that has the same frequency with the motion is applied. The motion and the applied gradient cause the phase contribution to the MR image (ϕ) at a given position vector ($\vec{r}$) and phase offset (θ) between the motion-encoding gradient and the motion.

$$\phi(\vec{r},\theta) = \frac{\gamma NT(\vec{G}\cdot\xi_0)}{2}\cos(\vec{k}\cdot\vec{r}+\theta) \tag{2-13}$$

where γ is the gyromagnetic ratio of the tissue protons, N is the number of gradient pairs for the motion sensitivity, T and G are the period and the amplitude of the motion-encoding gradient, respectively, ξ_0 is the peak amplitude of motion, and $\vec{k}$ is the wave vector. According to this equation, the vibrating tissue's MRI phase is proportional to its displacement [7].

A gradient-recalled echo with the RF pulse waveform, slice-selection gradient, frequency-encoding gradient, and phase-encoding gradient are commonly used in the MRE pulse sequence (**Figure 2.13**). Motion can occur in any direction, and so by manipulating the axes on which the motion-encoding gradients are applied, any motion can be encoded into the MR image's phase. In figure 2.13 as an example, only the motion in the direction of the frequency-encoding is sensitive to the image phase and encoded into it. This technique's capability of motion-encoding is highly sensitive, and therefore motion can be detected on the order of 100's of nanometers [7].

A wave image is a MR image that includes the propagating wave information in its phase. By using the motion-encoding gradients with opposite polarities subsequently, phase-difference

wave images are produced (**Figure 2.13**). They are then processed to eliminate the phase information which is not related to motion [7].

In figure 2.13, the temporal relationship (θ) between the induced sinusoidal waveform of motion and the motion-encoding gradient is also shown. The images of propagating wave in MRE experiments are obtained by changing the temporal relationship (θ) in following acquisitions, and this also allows the data processing through time. From the temporal data, information of the displacement at the applied mechanical frequency can be acquired for following processing, and false information of phase at other frequencies can be eliminated [7].

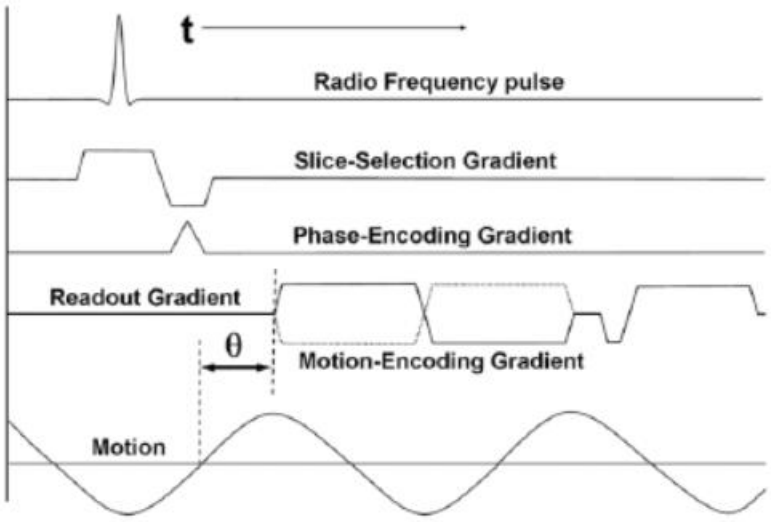

Figure 2.13. **MRE pulse sequence** Shown is an example of a gradient-recalled echo MRE pulse sequence diagram. A typical bipolar motion-encoding gradient (MEG) is shown (solid line) as well as the negative MEG (dotted line) used for phase-contrast imaging. The motion waveform and its temporal relationship (Θ) with the MEG are also shown. Adapted from "Magnetic Resonance Elastography: A review," by Y. K. Mariappan, K. J. Glaser, and R. L. Ehman, 2010, 23(5): 497-511, Clin Anat.

There are MRE pulse sequences based on gradient-recalled echo (GRE) shown previously, spin echo (SE), echo planar imaging (EPI), and balanced steady-state free precision (bSSFP) for different applications. These MRE pulse sequences can be designed to be sensitive to motion of a particular frequency by matching the frequency of motion-encoding gradient to that particular motion frequency. They can also be designed to reduce the echo time for

applications with short-T2 tissues by matching the motion-encoding gradient frequency to a particular multiple of the motion frequency which makes it less sensitive to motion [7].

CHAPTER 3

Theory

The fundamental theories used to estimate the isotropic and anisotropic stiffness for our study are presented in this chapter.

3.1. Isotropic Stiffness Estimation

The stiffness of soft tissue is related to the stress and strain of the material. The relationship between the stress and strain can be assumed to be linear due to the small displacements in MRE [11]. For anisotropic objects, the motion equation can be expressed as a tensor with complex quantities that are independent to each other. These independent complex quantities can be reduced to the Lamé parameters by the assumption of isotropy. The Lamé parameters in linear elasticity are λ and μ. The Lamé's parameter λ is related to the longitudinal strain and the shear modulus μ is related to shear (transverse) strain [7]. The relationship between stress and strain from the assumption of isotropy can be expressed by

$$\sigma_{ij} = 2\mu e_{ij} + \lambda \delta_{ij} e_{nn} \tag{3-1}$$

where the component of the stress tensor is expressed as σ_{ij}, δ_{ij} is the Kronecker delta, and repeated indices are implicitly summed over. e_{ij} is the strain tensor and can be defined in terms of the displacement tensor (u_{ij}).

$$e_{ij} = \frac{u_{i,j} + u_{j,i}}{2} \tag{3-2}$$

In equation 3-2, indices after a comma indicate differentiation. If these equations are substituted into the motion equation, the general harmonic motion equation in an isotopic and linearly elastic medium is obtained [11].

$$[\lambda u_{j,j}]_{,i} + [\mu(u_{i,j} + u_{j,i})]_{,j} = -\rho\omega^2 u_i \tag{3-3}$$

where ρ is the mass density of the object, and ω is the mechanical oscillation's angular frequency. The Lamé parameters are complex numbers as previously mentioned, and the imaginary part of the parameters represents attenuation for a viscoelastic medium [11].

The equation can be more simplified by additional assumption of local homogeneity. This assumption makes λ and μ single unknowns rather than functions of position. It makes the equation as an algebraic matrix equation. The direct inversion can solve this matrix equation locally [11].

$$\mu\nabla^2\boldsymbol{u} + (\lambda + \mu)\nabla(\nabla \cdot \boldsymbol{u}) = -\rho\omega^2\boldsymbol{u} \tag{3-4}$$

where **u** is a column vector. Since λ is much larger than μ in soft tissues, it is not practical for the simultaneous calculation of the two parameters. Therefore, by using bandpass filtering or curl filtering, the longitudinal wave motion can be filtered out to remove this λ effect [7].

Additional assumption can also be made in order to remove λ. One can assume that the variation of displacements corresponding to the longitudinal wave is slow, and therefore they can be neglected ($\lambda(\nabla \cdot u) = 0$). This assumption simplifies the equation 3-4 to a single vector equation in μ.

$$[\nabla^2\boldsymbol{u} + \nabla(\nabla \cdot \boldsymbol{u})]\mu = -\rho\omega^2\boldsymbol{u} \tag{3-5}$$

Furthermore, the assumption of incompressibility ($\nabla \cdot \boldsymbol{u} = 0$) can be made to simplify it to the Helmholtz equation,

$$\mu\nabla^2\boldsymbol{u} = -\rho\omega^2\boldsymbol{u} \tag{3-6}$$

Now, the terms that are related to components in the different orthogonal directions are decoupled. Since each component is responsible for the equation individually, measurements in only one sensitization direction are enough to determine μ. The direct inversion of the motion equations is then used to measure the wavelength and stiffness values.

3.2. Anisotropic Stiffness Estimation

In this study, waveguide elastography [10] was used to measure the anisotropic stiffness of healthy human brains. Romano et al has demonstrated the use of DTI to track the fibers in the brain and applying MRE to estimate anisotropic stiffness.

3.2.1. Waveguide Elastography

In waveguide elastography, DTI is first used to determine the vectors of the fiber pathways in which the elastic waves travel. Then, a spatial-spectral filter (Appendix A) is applied to determine the measured MRE first harmonic displacements field. Next, by using Helmholtz decomposition (Appendix B), the longitudinal and transverse components of the total field are separated. Then, as shown in the below equations the stiffness tensor is solved to determine the anisotropic stiffness coefficients.

An orthotropic model with nine elastic coefficients, as well as the filter in the three orthogonal directions determined by the local reference frame of the fibers and three additional off-axis orientations for pure longitudinal wave propagation, were used to demonstrate this approach (**Figure 3.1**). This approach provides a solution for the elastic coefficients that are in

line with the fiber pathways to allow for lower order anisotropic models that is shown as valid or approximate models when the elastic coefficients' redundancies are exposed.

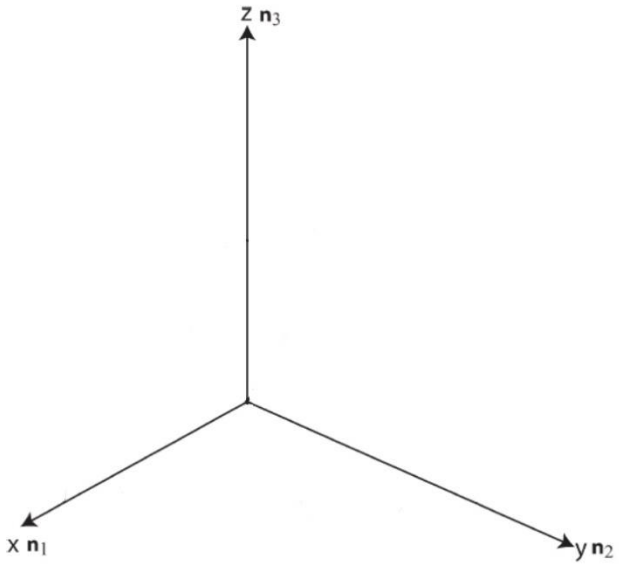

Figure 3.1.
Local reference frame of the fiber tracts illustrating the major orthogonal axes, $n_1,\ n_2, and\ n_3$.

Although there have been similar methods of solution for a completely Triclinic system with 21 elastic coefficients, Romano et al limited it to the Orthotropic model comprised of nine elastic coefficients (**Figure 3.2**) due to two reasons. First, the Orthotropic model consists of nine coefficients and is the highest order model. Therefore when using a directional filtering or multiaspect excitation to solve, it allows decoupling of the equation of motion for 1D Laplacians' simple solutions within the local reference frame for the solution of the six diagonal coefficients that are independent of one another as well as the off-diagonal coefficient subsequently averting from the ill-condition in the process of inversion. When a large disparity exists between the elastic coefficients or when signal to noise ratio is low, ill-condition happens. Unlike the Orthotropic model, components in the tensor locations such as $C_{14},\ C_{15},\ C_{16},\ C_{24},\ C_{25},\ C_{26},$

$C_{34},\ C_{35},\ C_{36},\ C_{45},\ C_{46}, and\ C_{56}$ of higher order models (Monoclinic model with 13 elastic coefficients and a Tricilinic model with 21 elastic coefficients) are nonzero. If these nonzero components are included, it is not possible for the motion equation to be separated for single coefficient solution using multiaspect excitation or directional filtering. The second reason is that most of the materials in nature do not have higher degrees of anisotropy than Orthotropy except for materials such as metals, glasses, semiconductors, particular crystals, and nanomaterials. Thus, it is reasonable to begin with the Orthotropic model with nine elastic coefficients for the degrees of anisotropy of human tissue. However, other models should be taken into consideration if the tissue is absolutely nonlinear, amorphous, or porous on a relevant scale [10].

For instance, a set of orthogonal unit vectors which define the orientation of the local rotating reference frame of waveguide is provided by DTI. The following equations represent the displacements within the local reference frame [10].

$$u_1 = n_{1,x}u_{SF,x} + n_{1,y}u_{SF,y} + n_{1,z}u_{SF,z} \tag{3-2a}$$

$$u_2 = n_{2,x}u_{SF,x} + n_{2,y}u_{SF,y} + n_{2,z}u_{SF,z} \tag{3-2b}$$

$$u_3 = n_{3,x}u_{SF,x} + n_{3,y}u_{SF,y} + n_{3,z}u_{SF,z} \tag{3-2c}$$

where $n_1(r'),\ n_2(r'),\ n_3(r')$ are the direction vectors of local eigenvectors taken from DTI and $u_{SF}(r')$ as filtered representation where r' is the local position vector [10].

For the diagonal of the orthotropic elastic tensor (**Figure 3.2**) contingent on monochromatic excitation, the following relationships can be provided.

Along $n_1(r')$,

$$C_{11}\frac{\partial^2 u_1^L(n_1)}{\partial x_1^2} = -\rho\omega^2 u_1^L(n_1) \tag{3-3a}$$

$$C_{66}\frac{\partial^2 u_2^T(n_1)}{\partial x_1^2} = -\rho\omega^2 u_2^T(n_1) \tag{3-3b}$$

$$C_{55}\frac{\partial^2 u_3^T(n_1)}{\partial x_1^2} = -\rho\omega^2 u_3^T(n_1) \tag{3-3c}$$

Along $n_2(r')$,

$$C_{66}\frac{\partial^2 u_1^T(n_2)}{\partial x_2^2} = -\rho\omega^2 u_1^T(n_2) \tag{3-4a}$$

$$C_{22}\frac{\partial^2 u_2^L(n_2)}{\partial x_2^2} = -\rho\omega^2 u_2^L(n_2) \tag{3-4b}$$

$$C_{44}\frac{\partial^2 u_3^T(n_2)}{\partial x_2^2} = -\rho\omega^2 u_3^T(n_2) \tag{3-4c}$$

Along $n_3(r')$,

$$C_{55}\frac{\partial^2 u_1^T(n_3)}{\partial x_3^2} = -\rho\omega^2 u_1^T(n_3) \tag{3-5a}$$

$$C_{44}\frac{\partial^2 u_2^T(n_3)}{\partial x_3^2} = -\rho\omega^2 u_2^T(n_3) \tag{3-5b}$$

$$C_{33}\frac{\partial^2 u_3^L(n_3)}{\partial x_3^2} = -\rho\omega^2 u_3^L(n_3) \tag{3-5c}$$

where $C_{11}, C_{22}, and\ C_{33}$ are the elastic coefficients along the three specific pure longitudinal mode directions ($n_1, n_2, and\ n_3$). C_{44}, C_{55}, and C_{66} represent the elastic coefficients along the transverse direction of each longitudinal direction. $u(n_1), u(n_2), and\ u(n_3)$ are the direction vectors filtered by the spatial-spectral filter and provided by a temporal Fourier transform. The parameters along the local axis are represented as $x_1,\ x_2, and\ x_3$. L and T represent the longitudinal and transverse components of the wavefield, respectively. These components are

separated by the Helmholtz decomposition. The complex elastic coefficients C_{11}, C_{22}, C_{33}, C_{44}, C_{55}, and C_{66} can be solved by dividing the right hand side by the 1D Laplacians [10].

$$\begin{bmatrix} C_{11} & C_{12} & C_{13} & 0 & 0 & 0 \\ C_{12} & C_{22} & C_{23} & 0 & 0 & 0 \\ C_{13} & C_{23} & C_{33} & 0 & 0 & 0 \\ 0 & 0 & 0 & C_{44} & 0 & 0 \\ 0 & 0 & 0 & 0 & C_{55} & 0 \\ 0 & 0 & 0 & 0 & 0 & C_{66} \end{bmatrix}$$

Figure 3.2.
The representation for the Orthotropic elastic tensor comprised of nine independent coefficients

CHAPTER 4

Methods

4.1. Subjects

This study included 23 healthy human volunteers with no history of any brain disorders. The informed consent with IRB approval for this study was provided by all volunteers. The range of the volunteers' age was from 18 to 62 years with an average age of 34.78 years.

4.2. Image Acquisition

4.2.1. Diffusion Tensor Imaging

A single-shot EPI sequence (TR: 7000 ms, TE: 87 ms) with 30 non-collinear directions was used to obtain diffusion tensor imaging (DTI) data for measurement of the fiber position. For DTI acquisition, resolution and slice positions of image were the same as in MRE. The total time of the acquisition was 4 minutes per volunteer. The tools (Eddy current corrector, BET, DTIFIT reconstruct) from the FMRIB Software Library (FSL) were used to calculate tensor and perform tractography of brains.

4.2.2 MRE

3T clinical MRI scanner (Siemens, Erlangen, Germany) was used for the MRE measurement in this research. A gradient-echo (GRE) pulse sequence was used. The frequency of 60 Hz was used for the pillow driver. MRE data composed of 52-57 adjacent transverse image slices with $2.5 \times 2.5 \times 2.5\ mm^3$ (128×128 pixels) isotropic spatial resolution and it was interpolated to $1.25 \times 1.25 \times 2.5\ mm^3$. A field of view (FOV) was 320×320 and a slice thickness was 2.5 mm. The image slices were parallel to anterior and posterior commissures of the brain. In figure 3.1, we display the MRI of a 26-year-old healthy female volunteer's brain with 52 adjacent image slices.

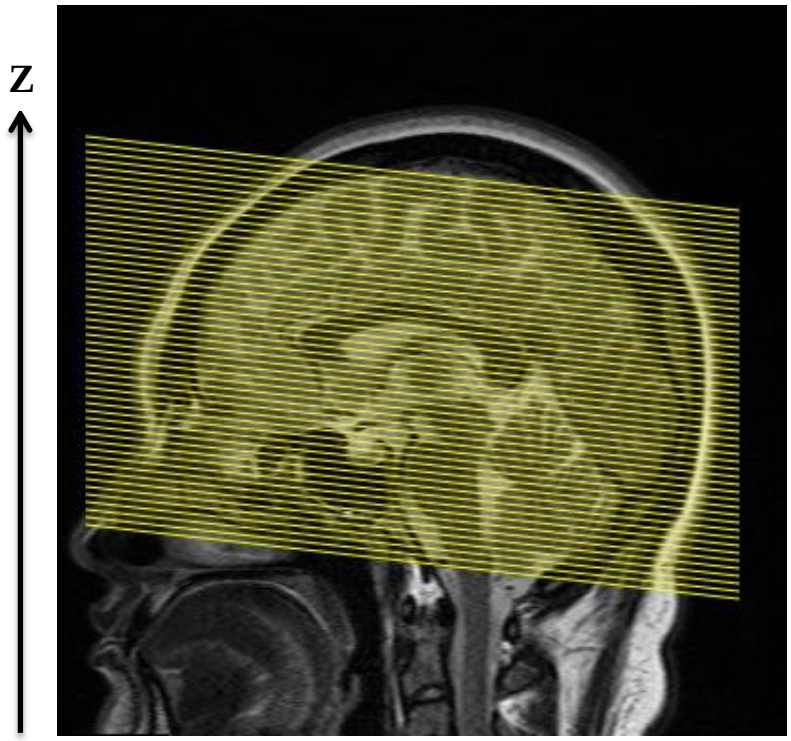

Figure 4.1. Positions of fifty two adjacent image slices used for MRE (slice thickness 2.5 mm).

4.4. Image Analysis

In this study, MRE-Lab software (Mayo Clinic, Rochester, MN, USA) was used to obtain the isotropic stiffness maps of the brain by using a 3D local frequency estimation (LFE) inversion algorithm. First, curl processing and a directional filtering operation were performed to remove the longitudinal wave components and reflected waves, respectively. Then, the first harmonic displacement field from all directions is further processed based on the weighted amplitudes to obtain isotropic stiffness map.

4.5. Region of Interests

ROIs for the corpus callosum and centrum semiovale in the brain were manually drawn in MRE-lab software with the help of Dr. Daniel Boulter who is an assistant professor in the department of Radiology at The Ohio State University.

CHAPTER 5

RESULTS

In this chapter, the results of isotropic stiffness of the whole brain, corpus callosum, and centrum semiovale for all 23 volunteers are presented. Additionally, the results of anisotropic stiffness of the three regions for 4 out of 23 volunteers are provided in this chapter.

5.1. Results of the Isotropic Stiffness Estimation

This section contains the results of the isotropic stiffness estimation. In figure 5.1, we show T2-weighted image (a) of a 26-year-old healthy female volunteer's brain and the snapshots of images indicating the propagating shear waves in the y-direction (b-e) of the brain corresponding to different time periods.

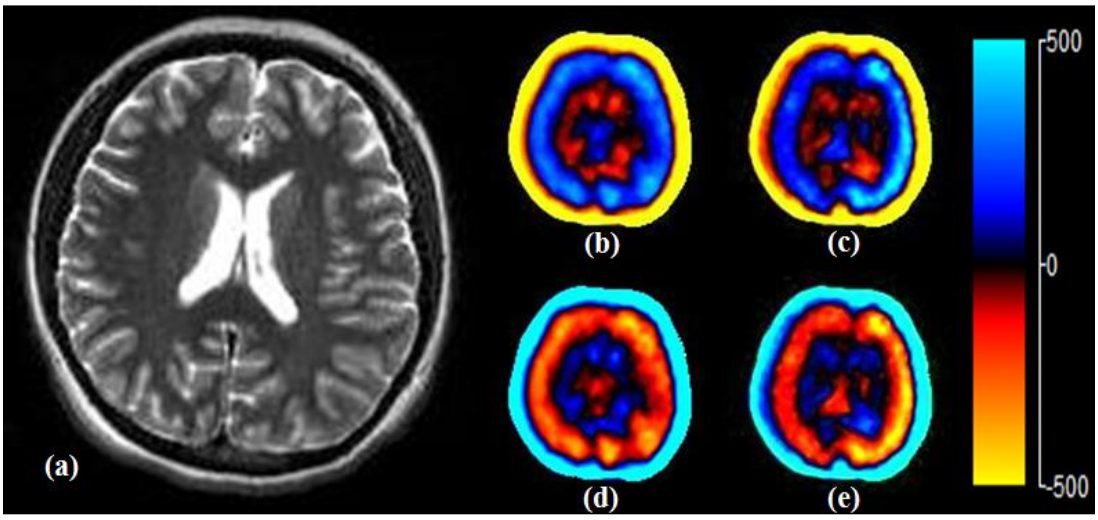

Figure 5.1. (a) T2-weighted anatomical MR image of the brain of 26-year-old female volunteer (volunteer #8). (b-e) The snapshots of propagating shear wave images of the brain in different time periods.

In figure 5.2, we present the elastogram of the whole brain, corpus callosum, and centrum semiovale. Figure 5.2(a-b) shows the whole brain's shear stiffness map in 30^{th} and 36^{th} slices, respectively, overlaid on the T2-weighted brain image. In figure 5.2(c), the stiffness map of corpus callosum (30^{th} slice) in brain is presented. Similarly, figure 5.2(d) displays the stiffness map of centrum semiovale in the brain (35^{th} slices). According to figure 5.2(b), the region of white matter shows higher isotropic stiffness than the region of grey matter which is the outer surface of the brain. For this particular volunteer, the mean isotropic stiffness of the whole region, centrum semiovale, and corpus callosum of the brain were 2.2917 ± 0.9642, 3.2966 ± 0.4218, and 1.8348 ± 0.3042, respectively.

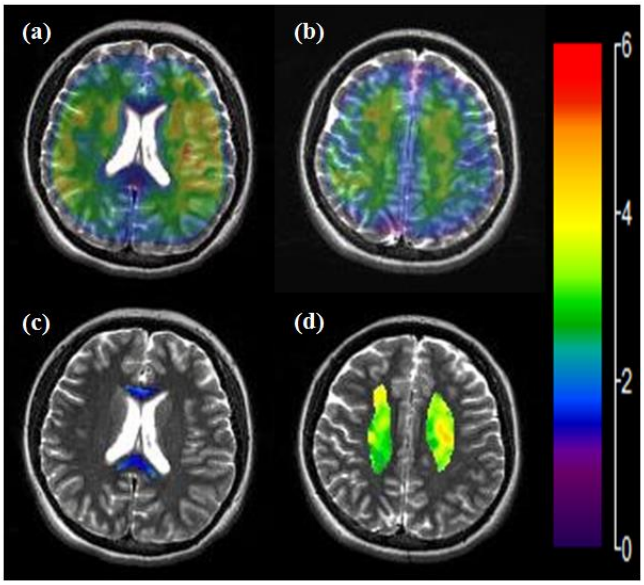

Figure 5.2. Elastograms of (a-b) the whole brain (slice #30 and #36), (c) corpus callosum (slice #30), and (d) centrum semiovale (slice #35).

Table 5.1 represents the mean isotropic stiffness of entire brains of the twenty three healthy volunteers in different ages with and without curl processing. The average brain stiffness

of all the volunteers is 2.1021±0.6262 kPa (without curl processing: 3.1686±0.8245 kPa). The range of the isotropic stiffness values of the volunteers is from 1.7035 to 2.3695 kPa. Figure 4.3 shows the slight decrease in the mean isotropic stiffness of the whole brain as the age of volunteer increases with the linear regression, y = -0.0053x + 2.2864. The R-squared value of the linear regression is 0.147.

		Without Curl Processing	With Curl Processing
Volunteers	**Age**	**Mean Isotropic Stiffness**	**Mean Isotropic Stiffness**
1	18	3.1846 ± 0.8125	2.2284 ± 0.6449
2	20	3.0796 ± 0.8099	1.9115 ± 0.5491
3	22	3.1749 ± 0.7197	2.1313 ± 0.5363
4	23	3.2375 ± 0.7085	2.2616 ± 0.5718
5	25	3.1598 ± 0.7596	2.1281 ± 0.6028
6	26	3.1958 ± 0.9254	2.0902 ± 0.6568
7	26	3.2049 ± 0.8549	2.1602 ± 0.6708
8	26	3.4248 ± 0.9642	2.2917 ± 0.7484
9	26	3.1963 ± 0.7651	2.0989 ± 0.5679
10	27	3.2427 ± 0.9489	2.1427 ± 0.7062
11	27	3.1122 ± 0.8195	1.9511 ± 0.5745
12	30	3.4337 ± 0.8519	2.3474 ± 0.6961
13	31	3.3245 ± 0.9971	2.1548 ± 0.6819
14	34	3.3746 ± 0.920	2.3695 ± 0.8026
15	39	3.1637 ± 0.9057	2.0291 ± 0.6432
16	41	2.5118 ± 0.7544	1.7199 ± 0.5195
17	42	3.4421 ± 1.0181	2.336 ± 0.7842
18	43	2.9883 ± 0.6427	2.0239 ± 0.5490
19	44	3.3064 ± 0.8999	2.1854 ± 0.6484
20	52	3.0850 ± 0.7286	2.0781 ± 0.5892
21	56	2.7975 ± 0.5793	1.8615 ± 0.4797
22	60	2.8808 ± 0.7222	1.7035 ± 0.5135
23	62	3.3559 ± 0.8565	2.1443 ± 0.6653

Table 5.1. Mean isotropic stiffness and standard deviation of whole brains of 23 volunteers.

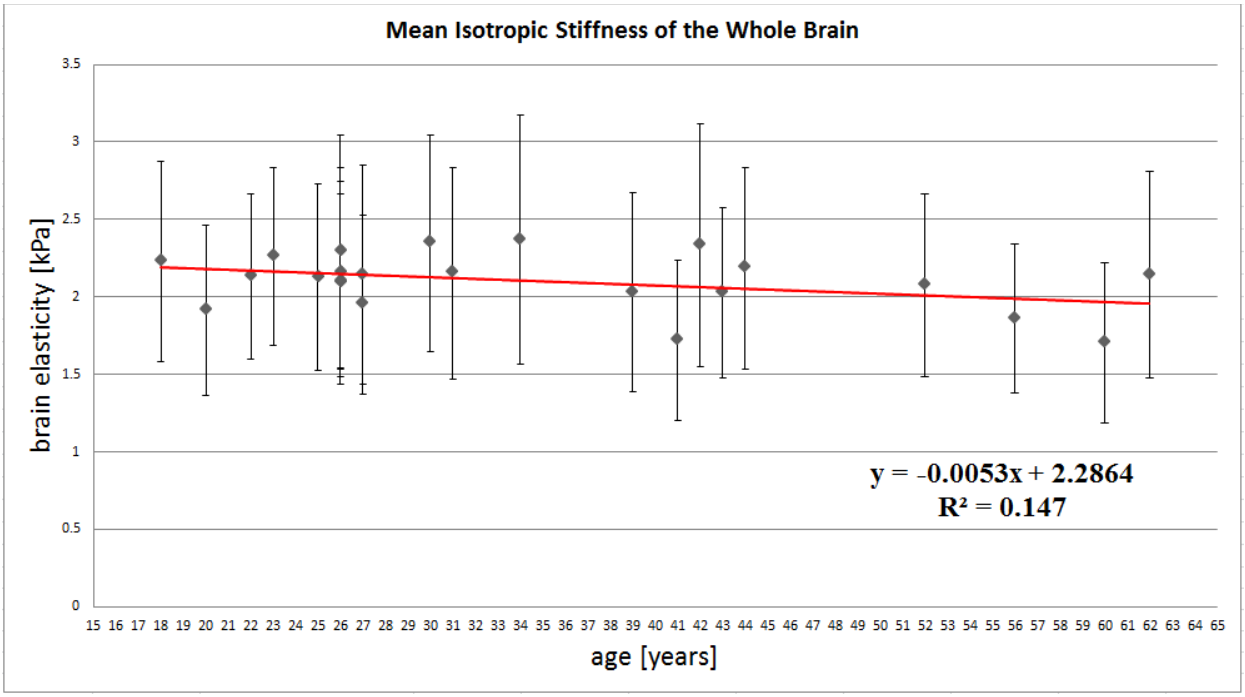

Figure 5.3. Mean isotropic stiffness measurements of the whole brains for the age study volunteers obtained at 60 Hz.

The mean isotropic stiffness of the centrum semiovale is slightly higher than the overall brain stiffness. According to table 5.2, the mean isotropic stiffness measurements of centrum semiovale from all volunteers are reported. The average stiffness in the centrum semiovales of 23 volunteers is 2.3534±0.4374 kPa (without curl processing 3.5720±0.5756 kPa). The range of the isotropic stiffness values of the volunteers is from 1.2766 to 3.2966 kPa. Similar to the result of the whole brain case, figure 5.4 shows the decrease in the mean isotropic stiffness of centrum semiovale as the age of volunteer increases with the linear regression, y = -0.0089x + 2.6635. R-squared value of the linear regression is 0.0551.

		Without Curl Processing	With Curl Processing
Volunteers	**Age**	**Mean Isotropic Stiffness**	**Mean Isotropic Stiffness**
1	18	3.9759 ± 0.8037	2.5004 ± 0.3376
2	20	2.8328 ± 0.5075	1.7374 ± 0.4317
3	22	3.8418 ± 0.3871	2.4864 ± 0.3353
4	23	3.7234 ± 0.6946	2.4584 ± 0.3221
5	25	3.3355 ± 0.5178	2.0509 ± 0.4857
6	26	3.4521 ± 0.4805	2.6370 ± 0.3785
7	26	3.9421 ± 0.7967	2.6004 ± 0.4324
8	26	4.3821 ± 0.4148	3.2966 ± 0.4218
9	26	3.7457 ± 0.5707	2.0823 ± 0.3685
10	27	3.9409 ± 0.7485	2.4952 ± 0.4246
11	27	3.7578 ± 0.4817	2.0608 ± 0.4599
12	30	3.5376 ± 0.4488	2.8057 ± 0.4045
13	31	3.8508 ± 0.6006	2.3657 ± 0.5372
14	34	3.5439 ± 0.6030	2.7320 ± 0.5684
15	39	3.2294 ± 0.5229	2.7143 ± 0.4097
16	41	2.1995 ± 0.5978	1.2766 ± 0.3749
17	42	4.5116 ± 0.7863	3.0236 ± 0.5838
18	43	3.2031 ± 0.4790	2.0729 ± 0.4306
19	44	3.7637 ± 0.5090	2.6108 ± 0.4324
20	52	3.4816 ± 0.5375	2.1245 ± 0.5083
21	56	3.0657 ± 0.4903	1.8477 ± 0.3765
22	60	3.0983 ± 0.6398	1.3717 ± 0.3379
23	62	3.7421 ± 0.6203	2.7757 ± 0.6981

Table 5.2. Mean isotropic stiffness and standard deviation of centrum semiovale of 23 volunteers.

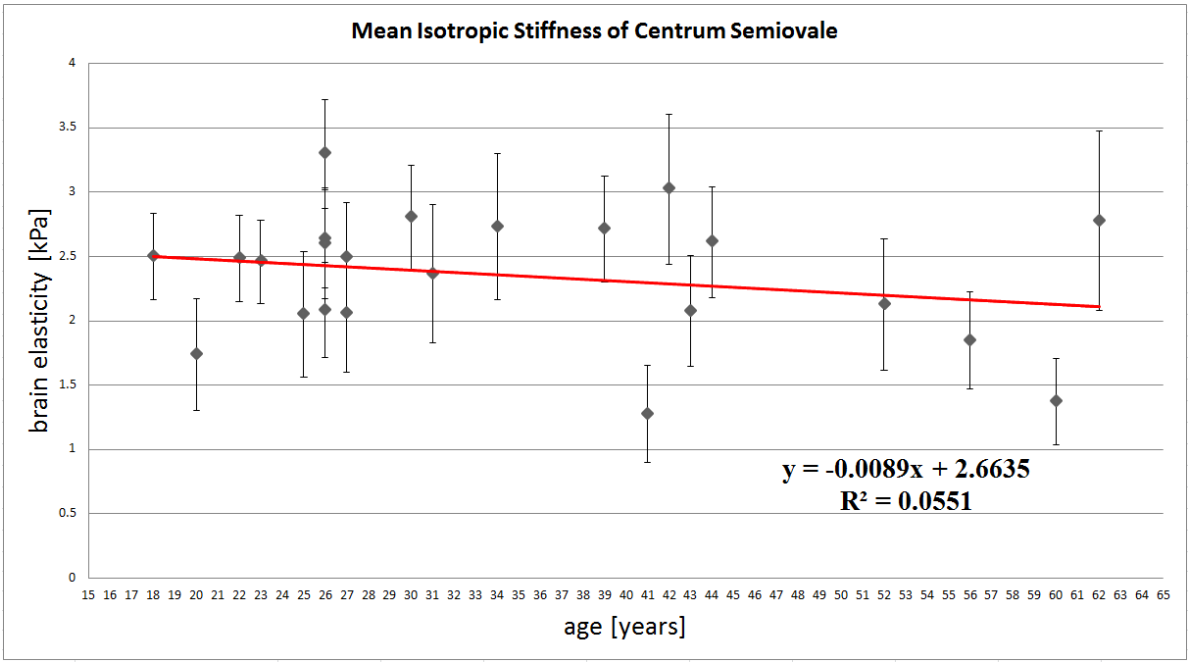

Figure 5.4. Mean isotropic stiffness measurements of centrum semiovale for the age study volunteers obtained at 60 Hz.

Corpus callosum showed lower stiffness estimates compared to the overall brain and centrum semiovale stiffness. Table 5.3 shows the mean isotropic stiffness measurements of corpus callosum from all volunteers. The average isotropic stiffness in the corpus callosum of all volunteers is 1.7535±0.3879 kPa (without curl processing: 3.0301±0.6029 kPa). The range of the isotropic stiffness values of the volunteers is from 1.1808 to 2.1122 kPa. According to figure 5.5, there is no significant change in the relationship between the mean isotropic stiffness of corpus callosum and the age of a volunteer. The linear regression of the stiffness measurements is y = -0.0002x + 1.7607. R-squared value of the linear regression is 0.0002.

		Without Curl Processing	With Curl Processing
Volunteers	**Age**	**Mean Isotropic Stiffness**	**Mean Isotropic Stiffness**
1	18	3.0126 ± 0.5970	1.9043 ± 0.4101
2	20	2.3319 ± 0.4466	1.1808 ± 0.2430
3	22	3.2662 ± 0.6353	2.0166 ± 0.3878
4	23	3.4717 ± 0.5584	2.0839 ± 0.4087
5	25	2.8558 ± 0.5395	1.6372 ± 0.4346
6	26	3.2554 ± 0.6364	1.8310 ± 0.3901
7	26	3.0194 ± 0.6651	1.6978 ± 0.4015
8	26	3.2456 ± 0.8512	1.8348 ± 0.3042
9	26	3.2359 ± 0.6999	1.7956 ± 0.3701
10	27	2.9294 ± 0.5650	1.7460 ± 0.3617
11	27	3.0613 ± 0.7360	1.6439 ±0.4030
12	30	3.0485 ± 0.6079	1.7858 ±0.4280
13	31	3.1713 ± 0.5760	1.6099 ± 0.3349
14	34	3.0219 ± 0.5174	1.7346 ± 0.5110
15	39	3.4016 ± 0.6019	1.8549 ± 0.3747
16	41	2.1565 ± 0.5243	1.3899 ± 0.3210
17	42	3.3802 ± 0.7231	1.9908 ± 0.4145
18	43	2.7828 ± 0.5112	1.5712 ± 0.4287
19	44	3.4712 ± 0.6582	2.1122 ± 0.4060
20	52	2.9584 ± 0.6139	1.7840 ± 0.3843
21	56	2.7145 ± 0.4820	1.6425 ± 0.3577
22	60	2.6659 ± 0.5734	1.6780 ± 0.4632
23	62	3.2331 ± 0.5475	1.8056 ± 0.3840

Table 5.3. Mean isotropic stiffness and standard deviation of corpus callosum of 23 volunteers.

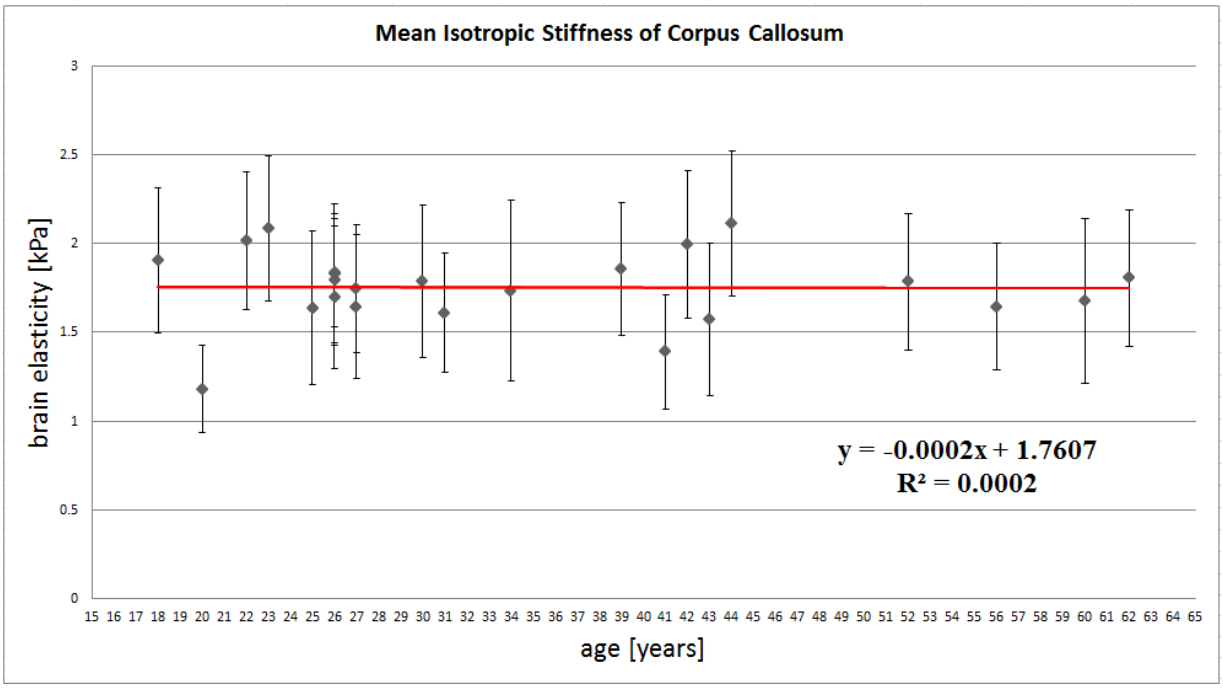

Figure 5.5. Mean isotropic stiffness measurements of corpus callosum for the age study volunteers obtained at 60 Hz.

5.2. Results of the Anisotropic Stiffness Estimation

In this section, the results of the anisotropic stiffness of the whole brain, centrum semiovale and corpus callosum for four volunteers (#8, #11, #20 and #23) are presented. The tables 5.6-9 display the anisotropic stiffness results of the whole brain, centrum semiovale and corpus callosum for each volunteer. The tables also include the isotropic stiffness results of the three regions for each volunteer as a comparison to the anisotropic stiffness results.

Parameter	Whole Brain	Centrum Semiovale	Corpus Callosum
C11	40.51 ± 1.72	41.68 ± 2.20	40.48 ± 1.32
C22	41.42 ± 4.50	40.91 ± 2.04	45.03 ± 5.15
C33	40.71 ± 2.33	42.50 ± 0.54	39.93 ± 0.55
C44	5.90 ± 1.12	5.94 ± 0.57	6.05 ± 0.31
C55	6.06 ± 0.85	5.84 ± 0.53	6.40 ± 0.18
C66	5.97 ± 0.95	6.09 ± 0.48	5.93 ± 0.37
Isotropic Stiffness	2.29 ± 0.75	3.30 ± 0.42	1.83 ± 0.30

Table 5.6. The anisotropic and isotropic stiffness of volunteer 8 (26-year-old)

Parameter	Whole Brain	Centrum Semiovale	Corpus Callosum
C11	40.59 ± 2.01	41.47 ± 1.49	40.59 ± 1.37
C22	41.74 ± 3.38	41.25 ± 1.78	44.42 ± 2.01
C33	40.67 ± 2.35	42.27 ± 1.84	40.06 ± 0.42
C44	5.82 ± 1.32	5.80 ± 0.74	5.98 ± 0.25
C55	6.05 ± 0.95	5.76 ± 0.64	6.36 ± 0.23
C66	5.89 ± 1.07	5.95 ± 0.64	5.90 ± 0.43
Isotropic Stiffness	1.95 ± 0.57	2.06 ± 0.46	1.64 ± 0.40

Table 5.7. The anisotropic and isotropic stiffness of volunteer 11 (27-year-old)

Parameter	Whole Brain	Centrum Semiovale	Corpus Callosum
C11	40.56 ± 2.73	41.45 ± 1.79	40.38 ± 1.15
C22	41.65 ± 4.66	41.17 ± 1.65	44.64 ± 4.27
C33	40.67 ± 1.95	42.21 ± 1.73	40.01 ± 0.47
C44	5.81 ± 1.34	5.92 ± 0.56	5.97 ± 0.28
C55	6.06 ± 0.92	5.89 ± 0.52	6.40 ± 0.18
C66	5.87 ± 1.11	6.03 ± 0.52	5.95 ± 0.35
Isotropic Stiffness	2.08 ± 0.59	2.12 ± 0.51	1.78 ± 0.38

Table 5.8. The anisotropic and isotropic stiffness of volunteer 20 (52-year-old)

Parameter	Whole Brain	Centrum Semiovale	Corpus Callosum
C11	40.55 ± 1.92	40.96 ± 1.54	40.63 ± 1.26
C22	42.00 ± 2.75	40.71 ± 1.19	44.52 ± 1.91
C33	40.57 ± 1.92	43.13 ± 1.52	39.99 ± 0.79
C44	5.71 ± 1.50	5.67 ± 0.60	5.90 ± 0.29
C55	6.00 ± 1.11	5.61 ± 0.58	6.35 ± 0.23
C66	5.77 ± 1.28	6.10 ± 0.51	5.83 ± 0.42
Isotropic Stiffness	2.14 ± 0.67	2.78 ± 0.70	1.81 ± 0.38

Table 5.9. The anisotrpic and isotropic stiffness of volnteer 23 (62-year-old)

The table 5.10 displays the average anisotropic stiffness of the whole brain, centrum semiovale and corpus callosum for the four volunteers with the average isotropic stiffness result.

Parameter	Whole Brain	Centrum Semiovale	Corpus Callosum
C11	40.55±2.1	41.39±1.8	40.52±1.27
C22	41.7±3.82	41.01±1.7	44.65±3.34
C33	40.66±2.14	42.53±1.4	40±0.56
C44	5.81±1.32	5.83±0.62	5.97±0.28
C55	6.04±0.96	5.78±0.57	6.38±0.21
C66	5.88±1.1	6.04±0.54	5.9±0.39
Isotropic Stiffness	2.12+0.64	2.56+0.52	1.77+0.37

Table 5.10. The average anisotropic and isotropic stiffness of the four volunteers (#8, #11, #20 and #23)

CHAPTER 6

DISCUSSION

In this study we used the mean isotropic stiffness of the whole brain, centrum semiovale and the corpus callosum in order to measure the change in elasticity with progression of age. Moreover, the further study of the anisotropic stiffness of the same regions was done on four out of twenty three volunteers.

Our results indicate that the isotropic stiffness of the whole brain and centrum semiovale slightly decreased with the progression of age, but the corpus callosum barely showed the stiffness change with age. Furthermore, according to our results, the average stiffness of the corpus callosum was lower than the whole brain and the centrum semiovale.

Unlike the result of the isotropic stiffness, the anisotropic stiffness of the whole brain, centrum semiovale and corpus callosum were very close to each other based on four volunteers. Additionally, there was no significant change observed in the anisotropic stiffness of the brain with age progression.

6.1. Regional difference in brain isotropic stiffness

Recent studies of the brain implied that the white matter has a higher stiffness than grey matter since white matter contains more neuronal fiber tracks than grey matter [14]. This pertains to the theory which explains that the mechanical makeup of the brain is comprised of soft-elastic neuronal fibers embedded in much softer glial cells [14]. Hence, a greater concentration of

neuronal fibers would display a higher stiffness. By using this theory we can suggest the possibility of why the centrum semiovale in our study showed an insignificantly higher elasticity compared to the whole brain. The centrum semiovale is a pure white matter region that is known to have numerous neuronal fiber tracks whereas the whole brain contains both the white matter and grey matter. However, this conclusion is limited since in order to accurately prove the theory that white matter is stiffer than the grey matter, a study comparing a pure white matter region and a pure grey matter region must be conducted.

Nevertheless, corpus callosum which is also considered a white matter structure displayed a minimally lower isotropic stiffness than the centrum semiovale according to our result. The difference in stiffness between the centrum semiovale and corpus callosum could possibly be due to the fact that we underestimated the stiffness of the corpus callosum by drawing the ROI that is smaller than its actual size. This could be also due to the slight variation in stiffness estimates stemming from our isotropic inversion technique.

6.2. Regional effects of aging on brain isotropic stiffness

For our study, we observed a decreasing trend in the mean stiffness of the brain with age progression. Although the decrease was not significant for all three regions, the isotropic stiffness of the centrum semiovale decreased the most when compared to the whole brain and the corpus callosum. This is presumably due to the degeneration of neuronal fibers of the white matter with increase in age as mentioned before.

The corpus callosum barely displayed a decrease in isotropic stiffness with the advancement of age despite the fact it is composed of pure white matter like the centrum semiovale. In a separate study, Dr. Jesús Pujol et al [16], observed that the corpus callosum can

actually grow up to the mid-20's. Current researches suggest that the corpus callosum is the least maturing neural network of the brain. From these two findings, we deduced that the reason why corpus callosum had a lower decreasing rate with age advancement as compared to the centrum semiovale was because the corpus callosum matured the latest.

6.3. Comparison with Previous Studies for the isotropic stiffness of the brain

Supposing the average stiffness of corpus callosum was 1.7535 ± 0.3879 kPa in our study, Johnson et al [13] on the contrary obtained 3.09 ± 0.39 for the average stiffness in the corpus callosum of seven healthy volunteers by using MRE. The difference may account for the fact that the sample size in our study is larger (23 volunteers) and the frequency in our study was 60 Hz as compared to 50 Hz used by Johnson et al (7 volunteers) [13]. However, we expect the stiffness to be increasing with increasing frequency in a viscoelastic material such as the brain; still the stiffness in our study is lower compared to Johnson et al even with higher frequency. The primary difference we postulate is the discrepancy in inversion strategies to estimate the stiffness. Nonlinear inversion (NLI) was used to estimate the average stiffness of corpus callosum in their study whereas we utilized a 3D local frequency estimation (LFE) inversion algorithm with curl processing and a directional filtering operation, which would ultimately provide differences in stiffness estimates and cannot be compared against each other. Moreover, with the help of the neurologist we manually drew the ROI for corpus callosum while Johnson et al acquired the mask for the corpus callosum using the ICBM-DTI-81 white matter atlas and parcellation map [13]. Any differences in ROIs can also attribute to variation in stiffness estimates. While our ROI

is mainly within the corpus callosum avoiding the edges, the use of an atlas in Johnson's study might have a possibility of including other regions corrupting the stiffness estimates of the corpus callosum.

Regarding the average stiffness of the full brain, Sack et al [14] obtained 3.25 ± 0.52 kPa which is higher than 2.1021 ± 0.6262 kPa for our study. The major factor for the difference may be caused by the different sizes of the ROI for the full brain in two studies. Sack and his team used four slices (slice thickness, 6 mm and resolution, 1.5mm x 1.5mm) around the left-right axis to account for the neck flexion, obtaining slices that were parallel to splenium and genu of the corpus callosum. Their ROI for the full brain only covers 24 mm of the middle of the brain; we on the other hand used 52-58 slices (slice thickness, 2.5 mm) to cover the entire brain. Conjointly, Sack et al used 1.5T clinical MRI scanner with 50 Hz for the MRE acquisition whereas we used 3T with 60 Hz [14].

According to the observation regarding age effect, Sack et al [14] showed a similar pattern in the mechanical properties of the brain. Sack's data also presented a decrease in stiffness of the full brain with advancement of age and we showed a similar trend in our study. Even though both studies show the decrease in the brain stiffness with age, the result of Sack et al shows a stronger correlation between decreasing brain stiffness and age propagation with R^2 =0.589. The difference can be accounted for by the fact that the number of subjects for their study is sufficiently higher than our subject number. Sack et al had 66 volunteers almost thrice the number of our volunteers with the age range of 18 to 72 years, which is also a wider range of age than what we have used. [14].

6.4. Limitations and Future Directions

The number of subjects used for the study was not sufficient enough to generalize the correlation between elasticity of brain and progression of age. There were a larger number of volunteers in their twenties than elderly subjects as well as young participants around the age of 18-20 years. This is why the R^2 value of our study was low compared to the R^2 value of Sack's study which comprised of 66 subjects [14]. Therefore, the small number of subjects and lack of elderly subjects in this study can limit the accuracy of the average brain stiffness and patterns of regional aging effects in the brain elasticity.

Likewise, the brain is a viscoelastic material that shows both viscous and elastic characteristics when undergoing deformation. Yet, in our study we assumed the brain to be purely elastic and we estimated the stiffness using LFE, which is considered to be robust to noise and has been used to report stiffness of the brain in an earlier study [16]. Due to the viscous characteristic of the brain, additional measurements such as the loss modulus and damping ratio are necessary to fully understand the stiffness in brain.

Human brain like some biological tissues is anisotropic in nature because it has structured fibers and exhibits different structural integrity in the direction of the fibers compared to transverse to them. Consequently, identifying the fiber tracks and determining the anisotropic stiffness is critical when trying to fully understand the brain properties. So, our study clearly needs to extend the research on anisotropic stiffness since it is mainly focused on the isotropic stiffness of the brain.

6.5. Further Investigation of Anisotropic Stiffness

In our study of the anisotropic stiffness, we have found no significant difference in the stiffness of the whole brain, centrum semiovale and corpus callosum. There was only a subtle difference between the isotropic stiffness of the corpus callosum and the centrum semiovale for each volunteer. Unlike our result from the isotropic stiffness, the anisotropic stiffness of the whole brain, centrum semiovale and corpus callosum came to be quite similar. Furthermore, there was no significant decrease in the anisotropic stiffness of the brain with age progression. Nevertheless, this conclusion is limited since we developed results for only four subjects. Therefore, an in-depth study of anisotropic stiffness should be conducted using more volunteers.

CHAPTER 7

Conclusion

To conclude, we utilized MRE to measure the mechanical properties of the specific regions of the brain: whole brain, centrum semiovale and corpus callosum. Amongst the three regions, the mean isotropic stiffness was higher in the centrum semiovale and the whole brain, whereas the corpus callosum had the least mean isotropic stiffness. Although we observed a slight decreasing trend in stiffness of the centrum semiovale and the whole brain, we barely saw a decrease in stiffness with age advancement in the corpus callosum.

Four out of the twenty three volunteers were measured for their mean anisotropic stiffness of the brain. Interestingly, the whole brain, centrum semiovale and the corpus callosum had a very similar stiffness unlike our isotropic stiffness study. Moreover, the result for the anisotropic stiffness did not show any significant stiffness change in the brain with the progression of age. Nevertheless, the anisotropic stiffness data for our study is not sufficient enough to see the effect of age since the result is based on only four volunteers.

APPENDICES

APPENDIX A

Spatial-Spectral Filter

The spatial-spectral filter separates only the vectors of waves propagating in the specific directions out of a complex wave field within a region of interest (ROI). Within a ROI, a forward 3D spatial Fourier transform is used for the vector and spectrum of a specific wave. A following inverse Fourier transform that uses the complex conjugate of the same spectrum is performed. As a result of this, vector components at each location along a specific pathway are provided, and it removes the other vector components [10].

The following forward and inverse Fourier transform pair is considered in order to explain the process above.

$$U(k) = \int dru(r)e^{-ik\cdot r} \tag{A1}$$

$$u(r) = \frac{1}{2\pi}\int dke^{ik\cdot r}U(k) \tag{A2}$$

where *k* is a wave vector and r is a three-dimensional spatial vector. Now, *k* is dependent on unit vectors at each location r' along a pathway, and this gives $k = kn_i(r')$ where k is a scalar and i = 1,N. The spatial-spectral filter representation of $u_{SF}(r')$ is defined as

$$U\big(kn_i(r')\big) = \int dru(r)e^{-ikn_i(r')\cdot r} \tag{A3}$$

$$u_{SF}(r') = \frac{1}{2\pi}\int_{I_k} dk e^{ikn_i(r')\cdot r'} U(kn_i(r')) \tag{A4}$$

In the equations A4, the interval of variation of k=$|k|$ is represented as I_k. The equations show the wave components which are produced along a certain direction in relation to the path of a waveguide represented by r', namely a spatial-spectral filter.

APPENDIX B

Helmholtz Decomposition

The Helmholtz decomposition is a way that separates a complex wavefield into longitudinal and transverse components. The vector decomposition can be found from a vector function *U* which is defined on R^3 [10].

$$\mathrm{U} = U_L + U_T \tag{B1}$$

$$\nabla \cdot U_T = 0, \qquad \nabla \times U_L = 0 \tag{B2}$$

$$U_T = \nabla \times \psi, \qquad U_L = -\nabla\phi \tag{B3}$$

In equation B3, ψ is a smooth vector function and ϕ is a smooth continuous scalar function. The following equations can be obtained from the equations above [10].

$$\nabla \cdot U = \nabla \cdot U_L = -\Delta\phi \tag{B4}$$

$$\nabla \times \mathrm{U} = \nabla \times U_T = \nabla \times \nabla \times \psi \tag{B5}$$

The solutions for $\phi(r_1)\ and\ \psi(r_1)$ are

$$\phi(r_1) = \int_{R^3} \frac{1}{4\pi|r_1 - r_2|}\left(\nabla_{r_2} \cdot U(r_2)\right) dr_2 \tag{B6}$$

$$\psi(r_1) = \int_{R^3} \frac{1}{4\pi|r_1 - r_2|}\left(\nabla_{r_2} \times U(r_2)\right) dr_2 \tag{B7}$$

Equations B6 and B7 can be used in the equation B3 [10].

$$U_T(r_1) = \nabla \times \int_{R^3} \frac{1}{4\pi|r_1 - r_2|}\left(\nabla_{r_2} \cdot U(r_2)\right) dr_2$$

$$= \int_{R^3} \nabla_{r_1}\left(\frac{1}{4\pi|r_1 - r_2|}\right) \times \left(\nabla_{r_2} \times U(r_2)\right) dr_2 \tag{B8}$$

$$U_L(r_1) = \nabla \int_{R^3} \frac{1}{4\pi|r_1 - r_2|}\left(\nabla_{r_2} \cdot U(r_2)\right) dr_2$$

$$= \int_{R^3} \nabla_{r_1}\left(\frac{1}{4\pi|r_1 - r_2|}\right) \left(\nabla_{r_2} \cdot U(r_2)\right) dr_2 \tag{B9}$$

If we take the Fourier transform of B8 and B9, the following equations are obtained [10].

$$U_T(k) = \Im_{r_1}\{U_T\} = i\frac{k}{k^2} \times \Im_{r_2}\{\nabla_{r_2} \times U(r_2)\} \tag{B10}$$

$$U_L(k) = \Im_{r_1}\{U_L\} = \int_{R^3} \Im_{r_1}\{\nabla_{r_1}\left(\frac{1}{4\pi|r_1 - r_2|}\right)\}\left(\nabla_{r_2} \cdot U(r_2)\right) dr_2$$

$$= \int_{R^3} i\frac{k}{k^2} e^{-ik\cdot r_2}\left(\nabla_{r_2} \cdot U(r_2)\right) dr_2$$

$$= i\frac{k}{k^2} \int_{R^3} \left(\nabla_{r_2} \cdot U(r_2)\right) e^{-ik\cdot r_2} dr_2$$

$$= i\frac{k}{k^2} \Im_{r_2}\{\nabla_{r_2} \cdot U(r_2)\} \tag{B11}$$

where $\Im_{r_1}\left\{\left(\frac{1}{4\pi|r_1-r_2|}\right)\right\} = \frac{1}{k^2}e^{-ik\cdot r_2}$ and $\Im_{r_1}\left\{\nabla_{r_1}\left(\frac{1}{4\pi|r_1-r_2|}\right)\right\} = i\frac{k}{k^2}e^{-ik\cdot r_2}$.

Using the derivative property of the Fourier transform for the equation B10 and B11, the following equations are obtained [10].

$$U_T(k) = -\frac{k}{k^2} \times (k \times U(k)) \tag{B12}$$

$$U_L(k) = -\frac{k}{k^2}(k \cdot U(k)) \tag{B13}$$

The displacements of the longitudinal and transverse components in real space are acquired by the inverse Fourier Transform of these equations [10].

References

[1] Katti G, Ara SA, Shireen A. Magnetic resonance imaging (MRI) – A review. International Journal of Dental Clinics. 2011; 3(1):65-70.

[2] Cho ZH, Jones JP, Singh M. Foundations of medical imaging. John Wiley & Sons, Inc. 1993.

[3] Nishimura DG. Principles of magnetic resonance imaging. Dwight G. 2010.

[4] O'Donnell LJ, Westin CF. An introduction to diffusion tensor image analysis. Neurosurg Clin N Am. 2011; 22(2):185-viii.

[5] Bihan DL, Mangin JF, Poupon C, et al. Diffusion tensor imaging: concepts and applications. Journal of Magnetic Resonance Imaging. 2001; 13:534-546.

[6] Alexander AL, Lee JE, Lazar M, Field AS. Diffusion tensor imaging of the brain. Neurotherapeutics. 2007; 4(3):316-329.

[7] Mariappan YK, Glaser KJ, Ehman RL. Magnetic resonance elastography: a review. Clin Anat. 2010; 23(5):497-511.

[8] Bernstein MA, King KF, Zhou XJ. Handbook of MRI pulse sequences. Elsevier Inc. 2004.

[9] Glaser KJ, Manduca A, Ehman RL. Review of MR elastography applications and recent developments. Journal of Magnetic Resonance Imaging. 2012; 36:757-774.

[10] Romano A, Scheel M, Hirsch S, Braun J, Sack, I. In vivo waveguide elastography of white matter tracts in the human brain. Magnetic Resonance in Medicine. 2012; 68:1410-1422.

[11] Manduca A, Oliphan TE, Dresner MA, Mahowald JL, Kruse SA, Amromin E, Felmlee JP, Greenleaf JF, Ehman RL. Magnetic resonance elastography: Non-invasive mapping of tissue elasticity. Elsevier Science B.V. 2001; Medical Image Analysis 5: 237-254.

[12] Marner L, Nyengaard JR, Tang Y, Pakkenberg B. Marked loss of myelinated nerve fibers in the human brain with age. J Comp Neurol. 2003 Jul 21; 426(2): 144-52.

[13] Johnson CL, McGarry MDJ, Gharibans AA, Weaver JB, Paulsen KD, Wang H, Olivero WC, Sutton BP, Georgiadis JG. Local mechanical properties of white matter structures in the human brain. NeuroImage. 2013; 79: 145-152.

[14] Sack I, Streitberger K-J, Krefting D, Paul F, Braun J. The influence of physiological aging and atrophy on brain viscoelastic properties in humans. PLoS ONE. 2011; 6(9): e23451. doi:10.1371/journal.pone.0023451.

[15] Kruse SA, Rose GH, Glaser KJ, Manduca A, Felmlee JP, Jack CR, Ehman, RL. Magnetic resonance elastography of the brain. Neuroimage. 2008 January 1; 39(1): 231-237.

[16] Pujol, J, Vendrell, P, Junque C, Marti-Vilalta JL, Cadevila A. When does human brain development end? Evidence of corpus callosum growth up to adulthood. Annals of Neurology. 1993; 34: 71-75.